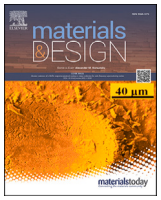
Materials & Design 241 (2024) 112889



Contents lists available at ScienceDirect

Materials & Design

journal homepage: www.elsevier.com/locate/matdes





Mechanistic machine learning for metamaterial fatigue strength design from first principles in additive manufacturing

Mustafa Awd [a,*], Lobna Saeed [b], Sebastian Münstermann [c], Matthias Faes [d], Frank Walther [a]

[a] Chair of Materials Test Engineering (WPT), TU Dortmund University, Baroper Str. 303, Dortmund, D-44227, Germany
[b] Crystallography and Geomaterials Research Group, Faculty of Geosciences, University of Bremen, Klagenfurter Str. 2-4, Bremen, D-28359, Germany
[c] Institute for Metal Forming, RWTH Aachen University, Intzestr. 10, Aachen, D-52072, Germany
[d] Chair for Reliability Engineering (CRE), TU Dortmund University, Leonhard-Euler Str. 5, Dortmund, D-44227, Germany

ARTICLE INFO

Keywords:
Density functional theory (DFT)
Functional grading
Machine learning (ML)
Fatigue strength
Cohesion energy
Additive manufacturing (AM)
Lifetime prediction
Bayesian statistics
Process monitoring
Artificial intelligence (AI)

ABSTRACT

Digital control in manufacturing processes produces significant amounts of metadata. The production process metadata, such as thermal and optical measurements, enables a higher degree of property grading than uninstrumented manufacturing and feedback for fault detection. This study explores how metadata can design fatigue-resistant structures using physically grounded models such as density functional theory, cyclic plasticity, and fracture mechanics that train machine learning algorithms. Machine learning models work very efficiently in their trained physical space. In comparison, mechanistic models are computationally costly for complex phenomena such as fatigue. We show how fatigue can be administered consistently at all scales by energy-based criteria and how a mechanistic function can be built based on this concept. The energy mechanistic function allows exact quantification of the effect of the existing flaws from manufacturing on fatigue lifetime under certain load boundary conditions. Since the mechanistic function is local and subscale to the prediction scale of the machine learning model, it can be used to build density functions for probabilistic regression of the fatigue property on the scale above. The analysis is applied to the selective laser melting process due to the availability of digital control and metadata generation during deposition.

1. Introduction

There are benefits to additive manufacturing (AM) over conventional subtractive manufacturing methods, but more structural qualification is needed for technical alloys' cyclic deformation and fatigue characteristics. Increasing high-cycle fatigue resistance in metallic materials under cyclic loads is essential for structurally demanding applications. Often, efforts to improve fatigue damage resistance using traditional strengthening methods and hierarchical nanostructural alterations are unsuccessful. However, physics-based methods appearing in the recent literature promise significant breakthroughs when coupled with high throughput machine learning and digital twinning techniques. In pure Cu, low-angle dislocation barriers are introduced at the nanoscale, improving tensile strength and fatigue limit. The increased fatigue life results from the high density of built-in low-angle dislocation cells, which reduces surface roughening and crack initiation [1].

The fatigue life of materials with minor flaws was estimated when subjected to multiple loads, and a notch factor and Murakami criterion calibrated the Fatemi-Socie, Smith-Watson-Topper, Susmel, and Lazarin critical plane models. Results facilitated comparison between life predictions for various materials, loadings, and fault geometries [2]. However, applying empirical fracture mechanics suffers from low transferability and poor integration when coupled with highly advanced digital techniques. The effects of post-overload fatigue crack growth (FCG) and its relationships to the fatigue cycle and stress intensity were evaluated. The findings indicated that residual stress (RS) contribution, with dependency behind the fracture tip and applied stress-intensity dependence in front of the crack tip, is a critical element for FCG rate without initial acceleration [3]. The residual stress and fracture closure affect the fatigue crack growth rate (FCGR) retardation caused by overload. The equivalent effective stress intensity factor range idea was developed to calculate the stress intensity factor (SIF) range reduction ratio to evaluate the knockdown component concerning steady-state growth. Plotted, fitted, and divided into closure and residual stress effects, respectively, were the size and scope of the overload-induced crack growth rate retardation [4]. Fatigue investigations on welded

* Corresponding author.
E-mail address: mustafa.awd@tu-dortmund.de (M. Awd).

https://doi.org/10.1016/j.matdes.2024.112889
Received 24 January 2024; Received in revised form 19 March 2024; Accepted 27 March 2024
Available online 8 April 2024
0264-1275/© 2024 The Author(s). Published by Elsevier Ltd. This is an open access article under the CC BY-NC license (http://creativecommons.org/licenses/by-nc/4.0/).

42CrMo4 steel led to a viable material for hydrogen transport infrastructure to see how fatigue fracture formation was aided by hydrogen. Results demonstrate considerable differences in testing methods and weld areas, with environments containing hydrogen showing almost an order of magnitude more excellent rates of fatigue fracture formation. Both testing methods revealed similar microstructural behavior, with martensite lath decohesion and intergranular fracture being detected. The heat-impacted zone demonstrated a higher vulnerability to hydrogen embrittlement [5]. The capturing of all of these fatigue physical phenomena does not support knowledge transferability to other fatigue problems without effective digitalization of the models. Digitalization can be established through sensor technology during manufacturing and service life by active data logging and transfer to servers that process this information under the pretext of fundamental physics of electronic structures and innovative machine learning techniques. Hence, the authors aim to introduce their mechanistic machine-learning technique in additive manufacturing under this framework.

In additively composed materials, surface, and bulk flaws were addressed using post-processing techniques. The main subject of the investigation was the impact of peening treatments on the fatigue performance of AlSi10Mg specimens used in V-notched laser powder bed fusion. A machine learning-based methodology found the relationships between residual stress, hardness, surface roughness, crack initiation site depth, and fatigue life. The findings indicated that deeper fracture initiation sites and better fatigue life are produced by increasing surface hardening and decreasing surface roughness. The improvement in fatigue life in the samples was also directly correlated with the depth of sub-surface fracture formation [6]. An innovative phase-field fracture framework based on fast Fourier transform (FFT) simulated fatigue cracks' microscale initiation and propagation and established a relationship between phase-field fracture and microstructural fatigue damage by defining a damage-driving force based on energy and dislocation density. The framework mimicked the first phases of fatigue cracking, forecasting crack directions, rates of growth, and sensitivity to microstructural characteristics [7]. The loading effect on fatigue cracks in specimens made of the aluminum alloy AA6082 (BS HE30) was correlated to crack morphology to comprehend crack closure and residual stress effects. The focused ion beam digital image correlation (FIB-DIC) approach assessed residual stress at key regions near fracture retardation sites. To determine the functions of fracture closure and residual stress effects, the results were compared with experimental data [8]. Prediction of fatigue fracture propagation was performed in aluminum alloy 7075-T7351 coupons subjected to military transport aircraft loading using FASTRAN v5.76. The highlight was the use of crack growth rate information for near-threshold prediction and the efficacy of FASTRAN for diverse crack growth scenarios. To accurately and reliably anticipate the formation of fatigue cracks across various structures, situations, and scenarios, engineers face issues when predicting fatigue crack growth under variable amplitude loading [9]. Machine learning was used to find control limits of fatigue strength of hybrid fatigue specimens manufactured by selective laser melting on wrought aluminum alloys. The methodology was accurate from low to very high cycle fatigue [10]. To explore fatigue crack propagation utilizing molecular dynamics (MD) and extended finite element method (XFEM), it was suggested to use a representative volume element (RVE)-based multi-scale method. The RVE model is constructed by fitting MD data with the Paris law model, and an atomic model of carbon steel plate was constructed. Considered were microstructural flaws such as vacancies and interstitial atoms [11]. Coronary stents could detect coarse grains parallel to the ingot axis according to their microstructure. The Tanaka-Mura model in the finite element method (FEM) was used in the study to simulate the fracture initiation process in a cyclic loading environment. The impact of grain size, orientation, and surface roughness on the fatigue life of stent components was investigated [12]. A fatigue life model based on unified mechanics theory was discovered through ultrasonic vibration experiments on samples of A656 grade steel, and it successfully predicted high cycle fatigue life without using empirical curve fitting. The model necessitated the derivation of an analytical thermodynamic fundamental equation that describes the mechanisms that caused entropy to be generated during the fatigue process. Due to its cumulative nature, entropy enabled the addition of all active mechanisms [13]. Lamellar microstructure and micro defects impact the fatigue performance of metal alloys. The crystal plasticity finite element method (CPFEM) considered stress and the parametric accumulative difference indicator (ADI) for intragranular accumulative deformation. A higher β lath and synchronized refining improved the lamellar microstructural effect, possibly improving the design and production of advanced metal alloy materials [14]. A CPFE-based computational approach that predicted creep-fatigue crack onset life reveals the grain-level damage mechanism. Using a flexible creep-fatigue damage summing method for conservative evaluation, a new life prediction approach was built and verified by strain-controlled testing in the GH4169 superalloy at 650 °C [15]. The fatigue response of additive manufacturing (AM) components was estimated in the article using machine learning techniques. It demonstrated the viability of physics-based ML methods for forecasting the fatigue response of AM parts using feed-forward neural networks and physics-informed neural networks. Additionally, they examined the connection between process variables and fatigue response [16]. By utilizing isotropic linear elastic fracture mechanics (LEFMs) boundary displacements, a molecular dynamic (MD) model of a crack in pure aluminum has been created. With a sinusoidal load and 15 or more loading cycles, the model simulated the formation of fatigue cracks in aluminum. The combination of dislocation emission and atomic separation resulted in the observation of crack advance [17].

In this article, the authors introduce a new approach to design components against fatigue damage from the first principles upwards in scale. We utilize established numerical methods in quantum and continuum mechanics and expand their usage by combining them with atomistic and fracture mechanics methods. We enhance the post-processing and data analytics of these models' outcomes by applying Bayesian and reinforcement learning, new to this fatigue damage-tolerant design community. Reinforcement learning is particularly suitable for the fatigue problem because, in analogy to rewarding the agent in the classical machine learning setup [18], we can reward the model here with the physical model in the mechanistic setup we introduce in this study. Because fatigue is a multi-scale, multi-parameter problem, studying it parametrically without data science techniques is computationally and experimentally expensive. Data science and, above all, machine learning can identify data patterns and predict design rules. Their advantage is that they are data hungry which we remedy in this manuscript by introducing the mechanistic concept. The combination of physical and Bayesian models compensates for the lack of physical knowledge from using data-driven methods alone. Therefore we shed light on the mechanistic transformation of machine learning models that get trained based on modeling data that are physically grounded. In the coming sections, we explain the methodology of how the design against fatigue damage to control meta properties can start early on with the manufacturing process by mechanistic machine learning.

2. Materials and methods

We would like to visually introduce the reader to an overview of the aims of this study through Fig. 1. We use multi-exposure treatments in selective laser melting of metallic powder to induce controlled microstructures with specific potential cohesion energy that can be consumed as mechanical work to accommodate the loads applied during fatigue loading. The latter, described by probabilistic regression, has inherently statistical characteristics induced by the microstructure's heterogeneity and hierarchy. The hierarchy gives rise to variations of potential energy that sum up to nonuniform fatigue strength, although the applied load is uniform in standard fatigue laboratory tests. Hence, the weakest link concept is a valid claim in fatigue design and has

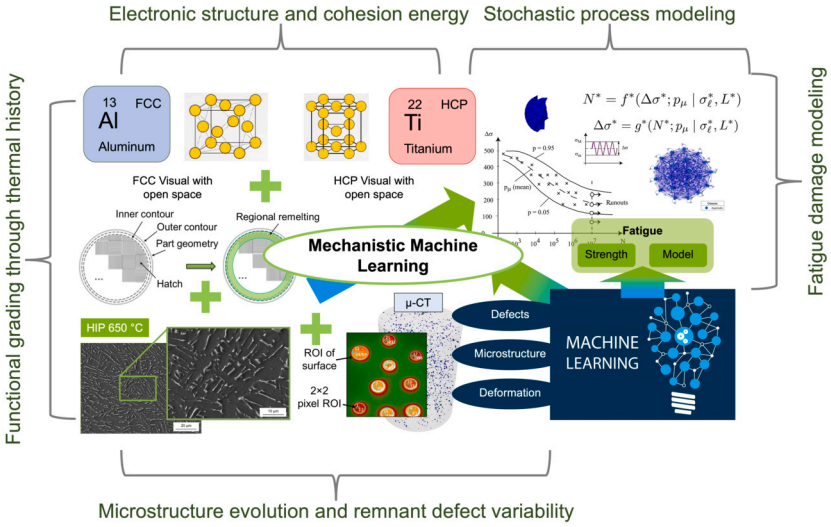


Fig. 1. Summary of the mechanistic machine learning strategy used in the current study which explains schematically the flow of physics-informed machine learning in the fatigue design problem.

been consistently successful in describing statistical properties of fatigue strength [19–23]. We utilize this concept in the comprehensive Bayesian model of heterogeneities presented in equation (51) that will be explained in detail in section reinforcement learning 2.5.

2.1. Experimental design

In this section we will introduce the process window we will train the model. That consists of specimens of Ti-6Al-4V built by selective laser melting in the vertical direction. One batch will be built by one laser exposure using optimized process parameters. The subsequent batches will have the standard first exposure plus a secondary exposure which will be varied. The variation will induce variation in microstructures and defect distribution. The data, which consists of the fatigue model prediction and distributions of the features, will be used to train and predict the machine learning model in the sections 2.2 through until 2.5. This section will also introduce the mechanical energy consumed by atomic damping as a microstructural origin for fatigue. The concept will be utilized in section 2.4.

The process window concerning laser scanning parameters is shown in Table 1. Ev stands for energy density, P for laser power, vs for scanning speed and D for spot size. The specimens were built on modified SLM 250 HL and SLM 500 HL systems for AlSi10Mg and Ti-6Al-4V alloys, respectively. They were all built in 90° orientation to the building platform. To induce an in situ heat treatment effect, a second exposure treatment was applied variably to control thermal history and cooling rates at specific contours. More details on the manufacturing technique can be found in [24]. Fig. 2 shows schematically the functional grading strategy implemented in this study to remelt already exposed layers aiming to improve local properties quantitatively by applying the mechanistic learning algorithm.

The schematic of the temperature measurements scheme and the principle behind it is shown in Fig. 3. The thermal history and heat accumulation were tracked during the remelting process by a wide field thermal camera from EQUUS (81k SM/M) to correlate layer by layer heat accumulation to the remnant porosity and its morphology. The calibration functions of the temperature were set by putting a powder and solid part sample into an oven that will quantify the temperature with thermocouples and surface radiation by the thermal camera. The setup was able to monitor a field of view of 100 × 100 mm^2 with 320 × 256 pixels and 300 frames per second such that multiple specimens were possible to track at the same time so differences between applied remelting parameter sets can be revealed. This thermal measurement will be used in the Bayesian model to achieve a probabilistic regression

Table 1
Local thermal control parameters of the in situ heat treatment of Ti-6Al-4V by selective laser melting.

Parameter	Power	Scanning velocity	Spot size	Energy density
Ti-6Al-4V platform-heated (PH) at 200 °C				
Batch	$(P; W)$	$(vs; mm/s)$	$(D; mm)$	$(Ev; J/mm^3)$
Standard	240	1,200	0.082	31.7
$Ev1$	200	1,000	0.082	31.7
$Ev2$	160	800	0.082	31.7
$Ev3$	120	600	0.082	31.7
$Ev4$	80	400	0.082	31.7
$P1$	80	1,200	0.082	10.6
$P2$	160	1,200	0.082	21.2
$P3$	320	1,200	0.082	42.3
$P4$	400	1,200	0.082	52.9
$vs1$	240	3,600	0.082	10.6
$vs2$	240	1,800	0.082	21.2
$vs3$	240	900	0.082	42.3
$vs4$	240	720	0.082	52.9
$D1$	240	1,200	0.116	31.7
$D2$	240	1,200	0.142	31.7
$D3$	240	1,200	0.164	31.7
$D4$	240	1,200	0.183	31.7

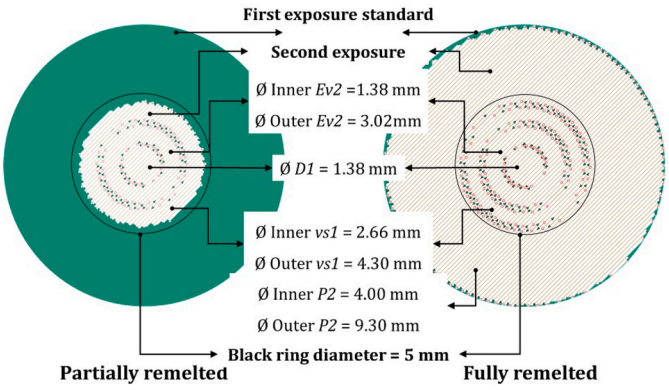


Fig. 2. Functional grading strategy of properties on the xy plane using the process parameters of Table 1.

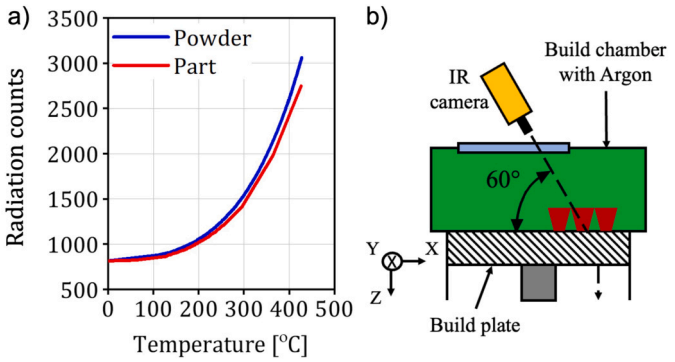


Fig. 3. Thermal imaging: a) measurement counts of powder and part; b) schematic illustration of the setup inside the chamber.

of the temperature profile of the laser parameter set with the resulting microstructure and fatigue strength. The thermal history is a measure of heat representing energy flow in the cohesion of the microstructure on the atomic scale in our analysis because thermal history defines the distortion of the primitive unit cell from the relaxed unit cell at temperature of absolute zero. The electronic structural configuration determines the cohesion in the bonds. Thus, the energy of the electronic structure is supposed to strongly correlate to the material's potential energy. Hence, fatigue strength, based on the energy method we will present later, can be correlated by energy conservation laws, and fatigue strength can be predicted in a physically grounded manner. During cyclic loading, the specimen accommodates a specific load applied by the corresponding displacement. This process of exerting mechanical work is an oscillatory motion with specific resolved kinetic and potential energy components. The energy during an oscillation can be expressed as [25]

$$E(R) = \frac{1}{2}\mu v^2 + \frac{1}{2}\kappa R^2 \tag{1}$$

where μ is the reduced mass (It is the effective inertial mass of a multi body problem), v is the velocity and κ is the stiffness constant. The stiffness constant is found through d^2E/dR^2 where R is the oscillation distance of one stroke. Depending on atomic, unit cell type, and molecular properties, an amount of internal damping (ID) is expected, which gives rise to plastic deformation [26]

$$ID = \frac{1}{2\pi}\frac{W_{diss}}{W_{el}} \tag{2}$$

where W_{diss} is the amount of energy lost in a given volume unit throughout one vibration cycle

$$W_{diss} = \oint \sigma \, d\varepsilon = \pi\sigma_0\varepsilon_0 \sin\phi = \pi J_2 \sigma_0^2 \tag{3}$$

and W_{el} is the maximum amount of elastic energy stored in a given volume

$$W_{el} = \int_0^{\sigma_0} \sigma \, d\varepsilon = \frac{1}{2} J_1 \sigma_0^2 \tag{4}$$

where J_1 and J_2 are the real and imaginary parts of the compliance J^*. The harmonic equation of motion governs the displacement amplitude x at the end of the fatigue specimen [27]

$$x(t) = x_m e^{-\beta t}\cos(t\sqrt{\omega^2 - \beta^2} + \Phi) + X_m \cos(\omega_\omega t + \phi) \tag{5}$$

where ω is the angular frequency, ω_ω the excitation frequency, β is the damping ratio. The amplitude is maximum at resonance frequencies. Fig. 4 shows the stress state along the ultrasonic specimen. The ultrasonic specimen was used for very high cycle fatigue testing. The high cycle fatigue testing up to 1E6 was carried out on a Schenck PC63M servohydraulic fatigue testing system with an Instron controller and 45 kN load cell. The vibration induces damage at specific rates that the Arrhenius equation can describe. This model expresses the rate of a process k in terms of temperature T subject to the conservation of energy if, for instance, the fatigue loading leads to heat dissipation which varies from a crystal lattice to another [28]

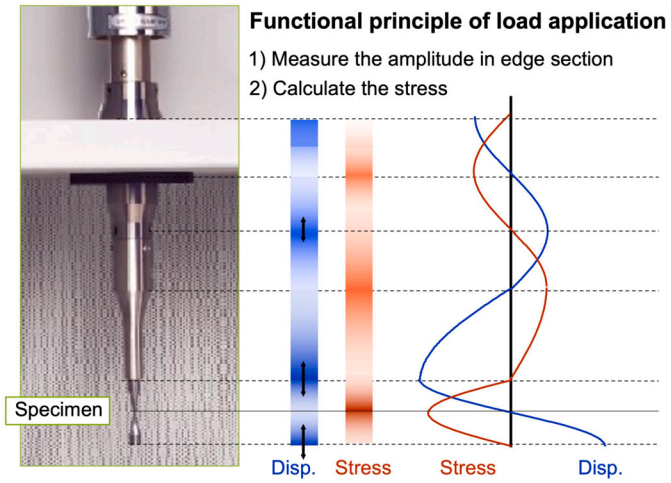


Fig. 4. Displacement-stress distribution along an ultrasonic fatigue specimen using ultrasonic resonance in the Shimadzu USF-2000a.

$$E(k) = Ae^{-B/T}, var(k), T \in X = [T_1, T_2], T_1 \geq 0 \tag{6}$$

where A is constant and B is a constant related to the activation energy of the fatigue damage process. An equilibrium constant K_{eq} can be related to the change in temperature T by the enthalpy ΔH^θ [29]

$$\frac{d\ln K_{eq}}{d(1/T)} = -\frac{\Delta H^\theta}{R} \tag{7}$$

where R is the universal gas constant. At this point, it becomes a primary task for us to estimate the potential energy of the concerning lattice structures numerically based on thermodynamically consistent calculations of the enthalpy of formation ΔH^θ which we will aim to achieve in the following sections.

2.2. Quantum mechanics

In the previous section 2.1, we discussed the atomic damping of the vibration energy of atoms, which, upon dissipation, leads to loss of cohesion and formation of the fracture surface. In this section, we will introduce atomistic simulation based on the density functional theory (DFT) to compute the cohesion energy in the respective phases of the tested alloys. In section 2.3 as well as section 2.4 we will compute the work per cycle and the cohesion energy of the microstructure. Thus, we can estimate the microstructure's capacity to accommodate the cyclic loading by deformation and how long it can endure. Therefore, fatigue data points be estimated model-based for the training of the machine learning model.

In quantum mechanics, or the *ab-initio* level, one can study explicitly the behavior of fundamental particles. On the other hand, predicting and understanding all features and aspects of these particles, especially while interacting, and mapping them onto mathematical formulations, is nearly an impossible task up to date. The success of density functional theory (DFT) over other classical and quantum computational methods comes from the balance between the predictability power and the computational tractability. In the Kohn-Sham (KS) framework, a fictitious system of non-interacting electrons is studied explicitly instead of the many-body wave function in Schrödinger equation (SE) in a self-consistent manner whereby the KS electron density that is calculated from KS equations must be approximately equal to the particle density that was used to construct the KS equations.

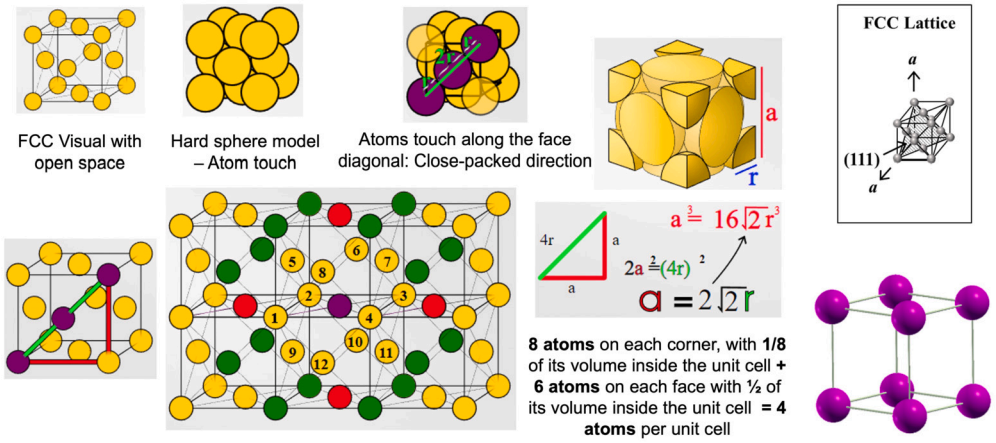


Fig. 5. Features of atomistic modeling of Al-based (FCC unit cell) alloys.

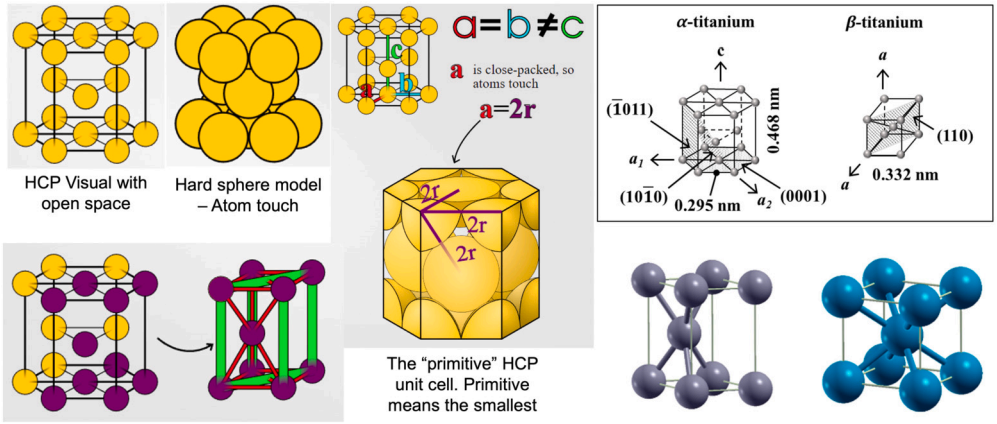


Fig. 6. Features of atomistic modeling of Ti-based (HCP unit cell) alloys.

The features and overview of the unit cell parameters involved in this atomistic DFT study are shown in Fig. 5 for Al-based (face-centered cubic – FCC unit cell) alloys and in Fig. 6 for Ti-based (Hexagonally closed packed – HCP unit cell) alloys. We start with constructing the structures of the elements and primary phases, which are Al and Ti, as shown in Fig. 5 and Fig. 6. This step is important for understanding the positions of atoms of each structure and for calculating equilibrium lattice constants and equilibrium c/a ratios (see Fig. 6), which will help construct the supercells used for all the following DFT calculations. Xcrysden software was employed to visualize the structures and phases throughout, as shown in Fig. 5 and Fig. 6. The crystallographic structural data, such as the space group, Wyckoff positions, number of atoms per unit cell, and lattice constants associated with each element and each phase, is detailed in [30]. Using the basis atoms, corresponding lattice vectors, and space groups, basis unit cells were constructed. Structural optimization to obtain minimum energies has been done by means of relaxing lattice constants and tetragonality ratio or c/a ratios for Ti (see Fig. 6); the calculated total energies versus the atomic volumes are plotted and given in Fig. 12. Further details on the theoretical background of these calculations can be found in Appendix A.

2.3. Continuum plasticity and damage

In sections 2.1 and 2.2, we introduced specimen manufacturing and atomic damping as a microstructural origin for fatigue failure and calculated the cohesion energy using DFT. However, to estimate fatigue strength we need to calculate the amount of dissipation that the specimen will endure under cyclic loading. We will perform this here using a truncated Fourier series based on cyclic plasticity theory, ductile damage, and model calibration from instrumented indentation. Later we will explain how to obtain the cohesion energies of complex microstructures in section 2.4 using trivial cohesion energies of simple phases from section 2.2.

The fatigue simulation is a dynamically complex process such that the implicit time integration in a cycle-by-cycle manner represents a computationally prohibitive task. Therefore, this study will depend on mapping the time-dependent displacement domain on the frequency domain such that a predetermined residual is reached in a Newton-Raphson scheme using a truncated Fourier series (TFS). Using a truncated Fourier series, the displacement boundary conditions and its residuals are [31]

$$\bar{u}(t) = u_0 + \sum_{k=1}^{n} [u_k^s \sin k\omega t + u_k^c \cos k\omega t] \tag{8}$$

$$\bar{R}(t) = R_0 + \sum_{k=1}^{n} [R_k^s \sin k\omega t + R_k^c \cos k\omega t] \tag{9}$$

where n stands for the number of terms in the Fourier series, $\omega = 2\pi/T$ and the u_0, u_k^s and u_k^c are the known displacement coefficients associated with each degree of freedom in the problem. The residual coefficients in equation (9) are obtained by tracking through the entire load cycle. A simple form of equation (5) is implemented for cyclic loading as follows [32]

$$dW_{damage} = \int_0^{\Delta\varepsilon} \sigma \, d\varepsilon \tag{10}$$

where σ is the applied load. $\Delta\varepsilon$ is the strain induced by the accumulation and saturation of the load and its associated displacement. Part of this work is irrecoverable and is the remanence of the supplied work after heat dissipation and deduction of resolved recoverable work

$$dW_{irrecoverable} = dW_{supplied} - (dQ + dW_{recoverable}) \tag{11}$$

It can also be decomposed into an inelastic part, heat, and damage such that the damage is proportional to the irrecoverable and the supplied work obviously

$$dW_{irrecoverable} = dW_{inelastic} - (dQ + dW_{damage}) \tag{12}$$

$$dW_{damage} \propto dW_{irrecoverable} \tag{13}$$

$$dW_{damage} \propto dW_{supplied} \tag{14}$$

If the potential energy of a specimen is consumed, fatigue failure is induced to preserve the electronic structure of the crystal lattice and form new fracture surfaces by realizing energy. Since the surface atoms have higher energy than bulk atoms, therefore, the fatigue lifetime of a structure can be trivially estimated by dividing the potential energy by the damage rate per fatigue cycle as suggested and validated by Ellyin [32] for the case of the rate-independent response as follows

$$Life = \frac{Potential\ energy}{Damage\ per\ cycle} = \frac{U_0}{dW_{damage}} \tag{15}$$

A more comprehensive, accurate representation following this concept will appear in the following lines after we include influences of heterogeneities. For this estimation, we will rely on instrumented indentation. In instrumented indentation, the relationship between indentation force and contact area with the indenter is [33]

$$H = \frac{F}{A_c} \tag{16}$$

where F is the indentation force and A_c is the contact area between the surface and indenter. The reduced Young's modulus E_c^* is a function of the slope of the withdrawal of the indenter S and disproportional to the square root of the contact area A_c [34]

$$E_c^* = \frac{S}{2}\sqrt{\frac{\pi}{A_c}} \tag{17}$$

However according to the first law of thermodynamics, the change in the internal energy of the materials being indented can be expressed as heat Q and work W [35]

$$\Delta U = Q - W \tag{18}$$

Assuming quasistatic deformation and absence of inertial forces, the indentation force F_p can be related to the pressure P across an equivalent projected diameter d_p of the contact area A_c along the unit vector $\hat{z}$ [36]

$$F_p = -\frac{\partial P}{\partial z}\frac{\pi d_p^3}{6} \tag{19}$$

assuming force equilibrium allows us to imply pressure P as a membrane stress σ in the material [37], hence

$$P = \sigma \tag{20}$$

which can be expressed in terms of cyclic hardening mechanisms [38]

$$\sigma = Isotropic + Kinematic \tag{21}$$

This expression trivially describes the state of the hysteresis loop in space. Both expansion and translation of the yield locus in space are induced by isotropic and kinematic hardening, respectively. The yield surface we aim to describe its evolution is itself described by

$$\mathbf{F} = \left(\frac{3}{2}(\boldsymbol{\sigma}' - \mathbf{x}') : (\boldsymbol{\sigma}' - \mathbf{x}')\right)^{\frac{1}{2}} - \sigma_y(\boldsymbol{p}) \le 0 \tag{22}$$

where $\boldsymbol{\sigma}$ is the current stress state and $\mathbf{x}'$ is the back stress in tensor form. The kinematic hardening is described in terms of plastic strain $\Delta\varepsilon^{pl}$ and back stress parameters as

$$\Delta\sigma - k = \frac{C}{\gamma}\tanh(\gamma\frac{\Delta\varepsilon^{pl}}{2}) \tag{23}$$

where k is a constant, C and γ are the parameters associated with this back stress. A component of back stress increment is described in terms of plastic strain as

$$dx = \frac{2}{3}Cd\varepsilon^{pl} - \gamma x|d\varepsilon^{pl}| \tag{24}$$

The combined isotropic and kinematic hardening model with one back stress will be [39]

$$\sigma = \sigma_0 + Q(1 - e^{-b\varepsilon^{pl}}) + \frac{C}{\gamma}(1 - e^{-\gamma\varepsilon^{pl}}) \tag{25}$$

where σ_0 is the initial size of the yield surface, Q and b are the isotropic hardening parameters. C and γ are the kinematic hardening parameters of the corresponding back stress component. The formation of fatigue intrusions and extrusions is predominantly induced by shearing in the principle resolved shear stress direction on the corresponding slip system; therefore, we will focus on using the Fatemi-Socie parameter in this study as we have ductile failures in bulk metallic specimens. The fatigue lifetime Fatemi-Socie model has a basic form as follows [40]

$$\frac{\Delta\gamma}{2}(1 + k\frac{\sigma_n^{max}}{\sigma_y}) = \gamma_f'(2N_f)^{c_0} + \frac{\tau_f'}{G}(2N_f)^{b_0} \tag{26}$$

where k is the Fatemi-Socie damage parameter that is empirically deduced as

$$k = \left[\frac{\gamma_f'(2N_f)^{c_0} + \frac{\tau_f'}{G}(2N_f)^{b_0}}{(1+\nu^e)\frac{\sigma_f'}{E}(2N_f)^b + (1+\nu^p)\varepsilon_f'(2N_f)^c} - 1\right]\frac{2\sigma_y}{\sigma_f'(2N_f)^b} \tag{27}$$

such that γ is the shear strain range, σ_y is the yield strength, c_0 and b_0 are the torsional fatigue strength, exponents, while c and b are the axial fatigue exponents, G is the shear modulus, σ_f' is the axial fatigue strength coefficient, ε_f' is the fatigue ductility coefficient. τ_f and γ_f are the axial and torsional fatigue strength and ductility coefficients, respectively. ν_e and ν_p are the elastic and plastic Poisson's ratios. At shear strain ranges below the macroscopic cyclic plastic strain limit, such as in very high cycle fatigue (VHCF), the inconsistency of the damage parameter approaching zero is avoided by multiplying the parameter by $(\Delta\gamma/2)(1 + (\sigma_n^{max}/\sigma_y)$ [41]. To homogenize the right-hand side of the equation, fatigue lifetime based on shear strain-life properties can be expressed by uniaxial loading using the relationships

$$\frac{\Delta\gamma}{2}(1+\frac{\sigma_n^{max}}{\sigma_y}) = ((1+\nu^e)\frac{\sigma_f'}{E}(2N_f)^b + (1+\nu^p)\varepsilon_f'(2N_f)^c)(1+k\frac{\sigma_f'}{2\sigma_y}(2N_f)^b) \tag{28}$$

$$\frac{\Delta\gamma}{2}(1+\frac{\sigma_n^{max}}{\sigma_y}) = ((1+\nu^e)\frac{\sigma_f'}{E}(2N_f)^b + (1+\nu^p)\varepsilon_f'(2N_f)^c) + k\frac{\sigma_f'}{4G}(2N_f)^b \tag{29}$$

Fig. 7 explains the flow of information in the Fatemi-Socie-based analysis of plastic damage in cyclic ratcheting accumulation. Fatigue models are built as digital twins of fatigue specimens by microcomputed tomography (μ-CT), and geometrical transformation from surface representation to finite element representation, which can be set in a boundary value problem that we will solve its deformation and stress by the truncated Fourier series method mentioned earlier. These digital twins aim to achieve control over the manufacturing process in an active property control technology. The nodal variables describe the damage state from specimen to specimen and predict fatigue lifetime in the Fatemi-Socie

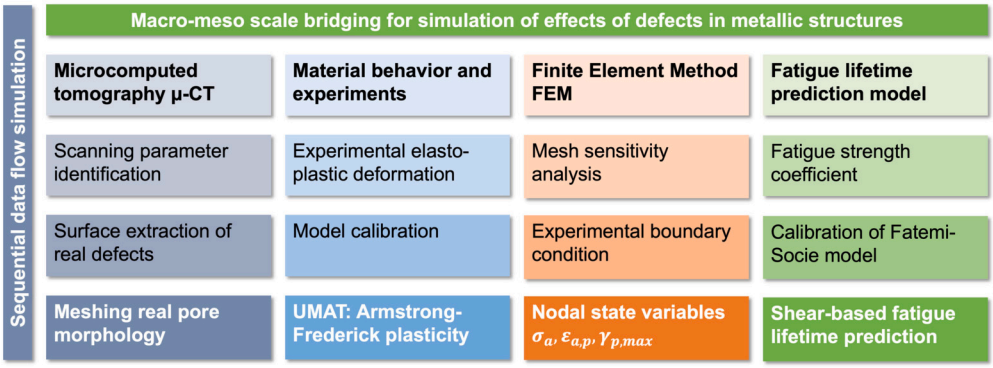


Fig. 7. Fatigue lifetime prediction based on damage of the continuum of the structure of interest [38].

model as a function of plastic and elastic properties. The outcomes provide the necessary $S-N$ data to fit the probabilistic regression fatigue lifetime model.

2.4. Fracture mechanics

The calculation of cohesion energy in section 2.2 cannot be trivially used for fatigue lifetime prediction. This calculation accounted only for simple lattices and did not yet include further cohesion mechanisms such as phase interfaces and grain boundary strengthening. Therefore, this section will explain the procedure to obtain more realistic cohesion energy values based on the kinetic failure of solids and use the values obtained from DFT as a first guess in a numerical scheme.

For a stressed body the time necessary for fracture according to the kinetic theory of failure of solids [42] is given by

$$\tau = \tau_0 e^{(U_0-\gamma\sigma)/RT} \tag{30}$$

where τ is the time to failure, τ_0 is a molecular vibration parameter, U_0 is the potential cohesion energy, γ is the lethargy of the microstructure, R is the gas constant and T is the temperature. We here estimate U_0 based on the first guess from DFT calculations of section 2.2 and instrumented indentation tests. The J-integral in an instrumented indentation test is [43]

$$J_{IC} \approx W_p \tag{31}$$

where W_p is the plastic work. The energy absorbed in the indentation is calculated as

$$K_{IC} = \sqrt{\frac{J_{IC}E}{1-\nu^2}} \tag{32}$$

where the toughness K_{IC} can be expressed independent of the geometry by the surface energy γ_p per mole [44]

$$K_{IC} = \sqrt{\frac{2}{\pi}\gamma_p E} \tag{33}$$

where E is the elastic modulus. When we recall that the electronic structure has a key role to play in the fracture of the matter and recall the kinetic equation of the fracture of solids equation (30) and interpret defects as loss of energy due to atoms having higher energy states on the surfaces of the defects than in the bulk of the materials. Thus, the effect of defects on fatigue strength can be initially formulated as

$$\begin{aligned} Fatigue\ life\ time &= \frac{Potential\ energy - Surface\ energy\ of\ defects}{Work\ per\ cycle} \\ &= \frac{U_0 - \gamma_s A_{defects}}{dW_{damage}} \end{aligned} \tag{34}$$

where γ_s is the surface energy per unit area. $A_{defects}$ is the projected area of the defects perpendicular to the loading direction. Therefore, the various geometric features of the defects, such as size, location, and morphology, could be accounted for. When the stressed volume does enough work, local fracture takes place as postulated by Irwin in [45]

$$G = -\frac{d\Pi}{dA} \tag{35}$$

where G is the energy release rate, Π is the potential energy of the stressed volume, A is the fractured surface. The J-integral is used to quantify this plastic energy in the contours ahead of the crack tip [46] as follows

$$J = \int_\Gamma \omega\, dy - T_i \frac{\partial u_i}{\partial x} ds \tag{36}$$

where ω is the strain energy density, T_i is the stress vector, u_i is the displacement vector and ds is the increment along the path Γ. To simulate this crack propagation into the specimen, we use the extended finite element method (XFEM) where the nodal shape functions give the displacement field after enrichment as [47]

$$u(x) = \sum_{I=1}^{N} N_I(x) \left[\vec{u_I} + H(x)\vec{a_I} + \sum_{\alpha=1}^{4} F_\alpha \vec{b_I^\alpha} \right] \tag{37}$$

where $N_I(x)$ is the nodal shape function, $\vec{u_I}$ is the displacement of the nodes, x is the coordinate and I is the element node label. The Heaviside function $H(x)$ is responsible for mitigating the singularity since it is a jump enrichment function of the $\vec{a_I}$ nodal degree of freedom (DOF) for jump discontinuity

$$H(x) = \begin{cases} 1 & if\ (\vec{x} - \vec{v}^*)\,\vec{n} \geq 0, \\ -1 & otherwise \end{cases} \tag{38}$$

The details on the crack propagation simulation can be found in [48]. The algorithmic implementation of the critical energy release rate fracture mechanics scheme within the XFEM is graphically represented in Fig. 8 on the basis of the energy release rate at the decohesion of the crack tip. The energy release rate is calibrated from the cohesion energy in equation (30). The reduction in fatigue strength due to the presence of defects as presented in equation (34) can be generalized to all heterogeneities in the following mathematical form

$$N(\sigma, U_0) = \frac{\int \ldots \int_V U_0(V) d^n V - \sum_{i=1}^{n} \gamma_{si} A_i}{dW_d^+ = \int_{cycle} (\sigma - \sigma_{ref}) H(\sigma - \sigma_{ref})\, d\varepsilon} \tag{39}$$

where N is the fatigue strength in cycles given a load σ the results in a strain ε while H is the heaviside function and σ_{ref} is equivalent to the critical resolved shear stress. U_0 is the potential energy stored in the material based on the ab initio calculations, which depend on the volume of the fatigue ensemble V within the structure (molecular dynamic

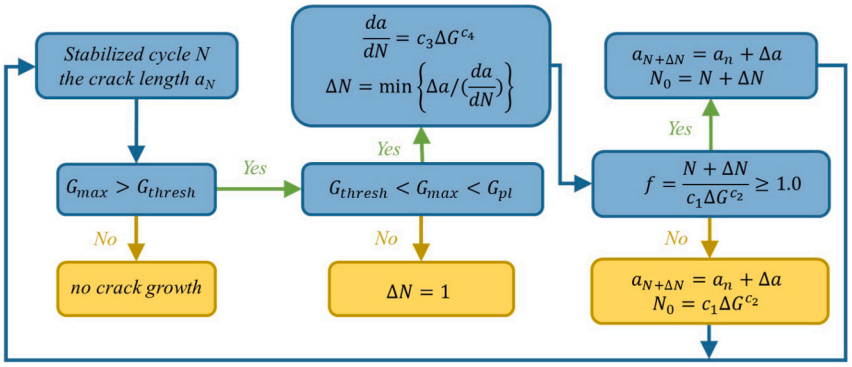


Fig. 8. Crack propagation workflow as implemented using XFEM in Abaqus [48].

calculations). γ_s is the surface energy per unit area of a heterogeneity A_i, which is not a sub-molecular heterogeneity.

2.5. Reinforcement learning

From sections 2.1 to 2.4, we showed our approach to fatigue lifetime prediction. The non-empirical approach can generate an enormous amount of synthetic fatigue data. Thus fatigue data points and the corresponding distributions of defects, microstructure, and thermal history can be used to train a probabilistic regression model in reinforcement learning. We will not need to split data for training and validation since we will use synthetic data for training and experimental data for testing and validation. The application of the reinforcement learning algorithm based on Weibull regression is introduced as follows. When equation (39) is solved for sufficiently numerous scenarios to calibrate the Fatemi-Socie model, the outcomes are used to train the following machine learning model for an arbitrary number of fatigue-related influences, as follows

$$Q(N|P(A_1), P(A_2), ..., P(A_n)) = \int \dots \int_N f(N|P(A_1), P(A_2), ..., P(A_n))\, d^n P(A_i) \tag{40}$$

Q is the probability distribution of N given the probability distributions of heterogeneities A^n. $f(N)$ is the mechanistic function of fatigue strength given distributions of heterogeneities $P(A_i)$ such as equation (39). The gamma function is defined by the form

$$\Gamma(\alpha) = \int_0^\infty x^{\alpha-1} e^{-x}\, dx, \quad for\ \alpha > 0 \tag{41}$$

If the density function of the failure rate of X is given by equation (42)

$$f(x;\alpha,\beta) = \begin{cases} \frac{1}{\beta^\alpha \Gamma(\alpha)} x^{\alpha-1} e^{-x/\beta} & \text{if } x > 0 \\ 0 & \text{elsewhere} \end{cases} \tag{42}$$

where $\alpha > 0$ and $\beta > 0$. The values of α and β change the central tendency and scatter of the distribution. The Weibull's cumulative distribution function (CDF) can be expressed in the closed form

$$F(x) = 1 - e^{-\alpha x^\beta} \quad for\ x \geq 0 \tag{43}$$

The stress-life model is derived based on the compatibility condition of Castillo and Cantelli [49]. In a Woehler field, the compatibility of the cumulative density function (CDF) of the lifetime N_f and the stress range $\Delta\sigma$ must be ensured such that the minimization law of the weakest link principle is valid

$$Q^*(N^*, \Delta\sigma^*) = E^*(N^*|\Delta\sigma^*) = F^*(\Delta\sigma^*|N^*) = q_{min}(N^*, \Delta\sigma^*) \tag{44}$$

It is implied that finding the compatible pairs of life and stress is a minimization optimization problem. The literature shows how the function is solved [50] leading to the log-dimensional Weibull model for which the maximum likelihood must be inversely minimized

$$Q(N, \Delta\sigma) = 1 - \exp\left(-\left(\frac{(\log N - B)(g(\Delta\sigma)) - \lambda}{\delta}\right)^\beta\right) \tag{45}$$

$$(\log N - B)(g(\Delta\sigma)) = constant$$

such that B is related to a fatigue lifetime threshold and C is related to a virtual fatigue limit. λ is the location parameter. These parameters are used for computational convenience and are not considered physical limits of fatigue since most recent literature on fatigue suggests that a limit does not exist [51,52]. However, the zero-percentile curve can be interpreted as the smallest number of cycles required to reach a fatigue failure for various stress levels, which is the value presented by the bias in lifetime or load. Hence the bias in a lifetime might be interpreted as the transition point between the macrostructural crack initiation and propagation until the arrest phase is finished [24]. In this case, a representation based on Gumbel CDF will be more rewarding because the heterogeneities causing fatigue failure are the largest heterogensities

$$Q(N, \Delta\sigma) = 1 - \exp\left(-\exp\left(\frac{(\log N - B)(g(\Delta\sigma)) - \lambda}{\delta}\right)\right) \tag{46}$$

$$(\log N - B)(g(\Delta\sigma)) = constant$$

Maximization of the log-likelihood of the Weibull model yields the expression [53,49,24]

$$L = -\sum_{i\in I_1\cup I_0} (\frac{N_i - \lambda}{\delta})^\beta + (\beta - 1)\sum_{i\in I_1} (\frac{N_i - \lambda}{\delta}) + \sum_{i\in I_1} \log\frac{\beta}{\delta} \tag{47}$$

with respect to λ, δ and β where I_0 and I_1 are the set of runouts and non-runouts respectively. Following the same footsteps, the maximized Gumbel likelihood will be [53,49,24]

$$L = -\sum_{i\in I_1\cup I_0} \exp(\frac{N_i - \lambda}{\delta}) + (\beta - 1)\sum_{i\in I_1} (\frac{N_i - \lambda}{\delta}) + \sum_{i\in I_1} \log\delta \tag{48}$$

We identify a joint probability function for a fatigue-related influence A_i for an arbitrary number of influences n. We generalize the concept introduced by [24] for porosity and microstructure. Hence, it can be formulated for a given load state $\Delta\sigma$ as

$$\mathbf{Q}(N, \Delta\sigma) = \sum_N \sum_{\Delta\sigma} f(N, \Delta\sigma|A_1, A_2, ..., A_n)\, \Delta^n A_n \tag{49}$$

in a discrete case, while in a continuous case

$$\mathbf{Q}(N, \Delta\sigma) = \int_N \int_{\Delta\sigma} f(N, \Delta\sigma|A_1, A_2, ..., A_n)\, d^n A_n \tag{50}$$

hence, the updates on beliefs of fatigue lifetime N_f and load $\Delta\sigma$ conjugates can be put in a posterior distribution using the prior form $\pi(N,\Delta\sigma)$ for an arbitrary number of influences A_n

$$\mathbf{Q}(N,\Delta\sigma|A_1,A_2,...,A_n)=\frac{\Pi_{i=1}^{n} f(A_i|N,\Delta\sigma)\,\pi(N,\Delta\sigma)}{\Pi_{i=1}^{n} g(A_i)} \tag{51}$$

where $g(A_i)$ is marginal probability of the fatigue-related influence of parameter A_i. For best local estimates of the conjugate at a given load level $\Delta\sigma^a$, we apply a 5-th order Taylor polynomial [31]

$$N_f(\Delta\sigma)\approx T_5(\Delta\sigma)=f(\Delta\sigma^a)-f'(\Delta\sigma^a)(\Delta\sigma-\Delta\sigma^a)+ \frac{f''(\Delta\sigma^a)}{2!}(\Delta\sigma-\Delta\sigma^a)^2+...+\frac{f^5(\Delta\sigma^a)}{5!}(\Delta\sigma-\Delta\sigma^a)^5 \tag{52}$$

Awd et al. [52] formulated a Monte Carlo estimate of the conditional distribution of a fatigue-related influence given a specific fatigue lifetime as follows

$$E[g(A_i)|N]\approx\frac{1}{S}\sum_{s=1}^{S} g(A_i^{(s)}) \tag{53}$$

sampling continues until saturation and the parameters of equation (45) are updated based on the reward function

$$r=\frac{p(A_i^*|N)}{p(A_i^{(s)}|N)}=\frac{p(A_i^*|N)p(A_i^*)}{p(N)}\frac{p(N)}{p(N|A_i^{(s)})p(A_i^{(s)})}=\frac{p(A_i^*|N)p(A_i^*)}{p(N|A_i^{(s)})p(A_i^{(s)})} \tag{54}$$

the error estimation minimizes the following expression using the simplex algorithm [54], if gradients are not possible to obtain analytically

$$L\left(N_f(A_i),N_f(U_0)\right)=\left(N_f(A_i)-N_f(U_0)\right)^2 \tag{55}$$

where $N_f(A_i)$ is the resulting fatigue lifetime based on statistical learning compared against the resulting experimentally-validated fatigue lifetime based on the physical potential energy concept. We will solve this simplex optimization problem linearly using the simplex algorithm, an iterative method introduced by Dantzig [54]. Hence, the problem is to be formulated as

$$\begin{cases} max(or\ min)[Z(y)=c^*y] \\ My=b \\ y\geq 0_{\mathbb{R}^n} \end{cases} \tag{56}$$

where $c\in\mathbb{R}^n$, $M\in\mathbb{R}^{m\times n}$ are beforehand fixed data. By solving a linear system of equations $M=yb$, we can obtain a solution of the form $\begin{pmatrix} B^{-1}b \\ 0_N \end{pmatrix}$. Therefore it is a global optimum that is a basic one [55]. Hence, the machine learning strategy applied here is a multilayer strategy of deeply interconnected regression schemes that apply high-dimensional integration by the Metropolis-Hastings Monte Carlo algorithm.

3. Results and discussion

3.1. Observable properties

The selective laser melting process induces unique microstructure characteristics in addition to the defects, which are unique compared to conventionally synthesized Ti-6Al-4V. Fig. 9 shows two magnifications of the microstructure under optical microscopy. Dominant prior β grains are observed in the build-up direction consistent with literature [56,57] and similar to electron beam melting with less pronounced texture [58]. This anisotropic texture is responsible for lower fracture strain according to [59]. In the current study, the in situ heat treatment presented in Table 1 leads to a significantly observable modification in the prior β grain morphology and width. The microstructure modification will change the cohesion energy and adjust fatigue strength locally. The scheme described in sections 2.2, section 2.3 as well as section 2.4 will be used to generate synthetic data points from these. Modified microstructures to train the machine learning model in section 2.5 and predict fatigue strength with further modifications in micros sutures and defect status. Moreover, the outcomes of the model suggest that the model can be used to design fatigue-resistant microstructures from the online measured data during processing. Hence, a significant influence on both quasistatic and fatigue properties was expected. It was proven by a cyclic instrumented indentation in the first cycle and subsequent cyclic hardening parameters. Significant microstructure modification indicated by the variability of the width of the prior β grain as shown in Fig. 9 led to control of elastic modulus, fracture toughness, cyclic plasticity parameters, and fatigue strength.

Inside the prior β grains, the strain localizes itself along the 45° α lath [60]. Hence, localization plays a critical role in fracture and the short microstructural crack propagation inside the prior β grain is a mechanism for crack retardation by grain boundary strengthening [61]. However, once this boundary is overcome we observe a microscopic drop in the slope of the stress-strain curve, as in Fig. 10a. After an initial hardening modulus beyond the elastic limit, the hardening modulus becomes negative, following the extension of the crack to other prior β grains. In the instrumented indentation test in Fig. 10b, a decrease of the slope of the unloading modulus ensues with cycles being added on the same indentation. Assuming a similar mechanism in the indentation, the load accommodation is transferred from within the prior β grain to the neighboring ones. This is a primary task of the microstructure designer to strengthen the prior β grain boundary to the maximum possible since this represents the extent of functional structural bearing capacity.

3.2. Lattice parameter energy

In additively manufactured bulk alloys, residual porosity has been identified as stress raisers [62–65] where models are being developed to capture the crack initiation effect that starts at these internal defects [66–68] and to differentiate between bulk and subsurface influences [69,70]. Most of these methods are based on fracture mechanics and the Murakami concept [71,72]. In contrast to linear elastic fracture mechanics, another methodology also attempted studying the local plastic deformation at defect roots [38] such as crystal plasticity methods [73,7,74]. A few has adopted an energy-based approach [75] similar to the one described here, and to the authors' knowledge, none has included atomistic effects in AM structural modeling except a previous publication of the authors [76]. The trivially calculated energy from section 2.2 is coupled with the theory of kinetic failure of solids in section 2.4 to obtain real microstructure-relevant cohesion energy. In this manner, the cohesion energy accounts for further microstructural strengthening mechanisms such as grain boundary strengthening and phases interfaces in addition to the trivial interatomic forces coming out of the primary phase calculations of DFT. The authors already demonstrated how coupling an efficient machine learning modeling with a proper phenomenological model can significantly enhance numerical techniques' predictive power through a comprehensive literature review [77] of empirical and numerical models and numerical solvers of fatigue damage mechanisms. The authors then couple these aspects of the literature by considering the variability of porosity in the specimens deposited through the plan in Table 1. We scan the specimen in the X-ray computed tomography and build density functions of porosity distributions based on Fig. 11 in addition to the distributions of microstructure based on Fig. 9. These distributions of porosity feed quantitatively in equation (39) and probabilistically in equation (40). Quantitatively they are used in equation (39) to deduce the actual potential energy of a fatigue specimen based on the microstructural potential energy estimated in equation (30) from the first guess made in the DFT calculation in equation (64). That is demonstrated graphically in Fig. 12. Fig. 12a shows an energy volume curve based on the DFT calculation, representing an utterly relaxed crystal lattice with an almost zero magnitude stress tensor. However, in the real specimens

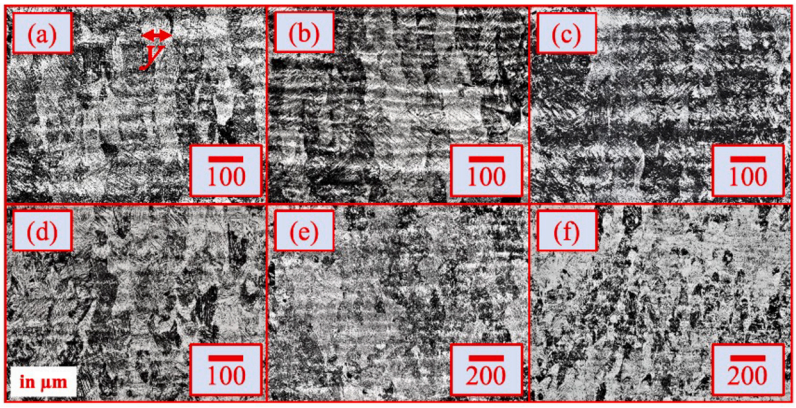


Fig. 9. Microstructure of SLM Ti-6Al-4V in first standard exposure parameters according to Table 1 showing the width y of a prior β grain as the microstructural parameter of interest. (a) – (f) represents a cross-section of the specimen at various locations with various magnifications to visually indicate the variability of the microstructure under the same scanning parameters.

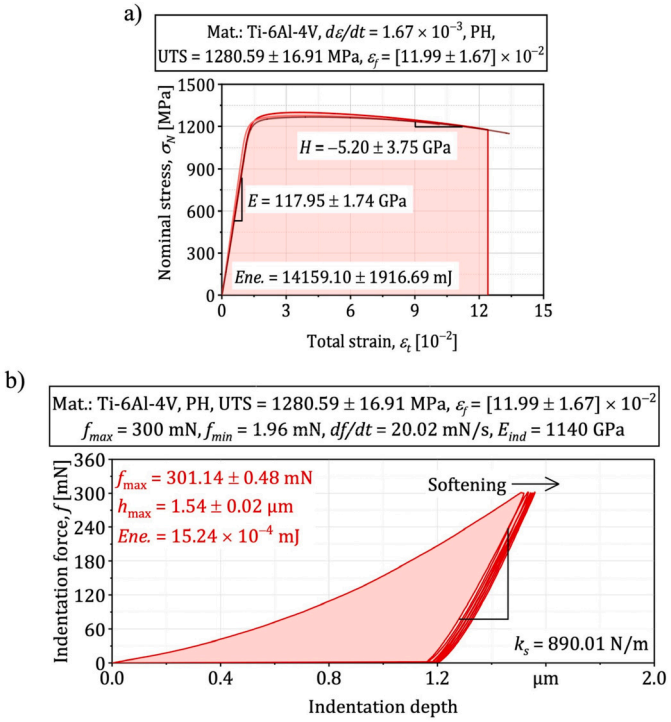


Fig. 10. Quasistatic properties of SLM Ti-6Al-4V in first exposure parameters: a) Tensile test; b) Ultramicro instrumented indentation; Mat.: Material; PH: platform-heated; UTS: Ultimate tensile strength; ε_f: Fracture strain; $\sigma_{a,start}$: initial stress amplitude in LIT; f: frequency; R: stress ratio; $d\sigma_a/dN$: rate of increase of stress amplitude; $\sigma_{a,f}$: failure stress amplitude in LIT; $\varepsilon_{a,f}$: failure strain amplitude in LIT.

and due to more complex interactions in the crystal and the superlattice (periodic structure of phases), the unit cell experiences a degree of distortion and volume change under an amount of residual stress. The deduced energy volume curve (MD corrected based on the theory of the kinetic failure of solids; equation (30)) is shown in Fig. 12b. Table 2 states the energy and lattice parameters of the SLM Ti α phase under the processing parameters of Table 1.

3.3. Cyclic deformation

The constitutive behavior of ductile materials is not stable throughout the fatigue loading regimes from low to high cycle fatigue; it is rather dynamic stress-strain behavior. In low cycle fatigue, where loads are high and nearer to the yield of the specimen, the relatively wide

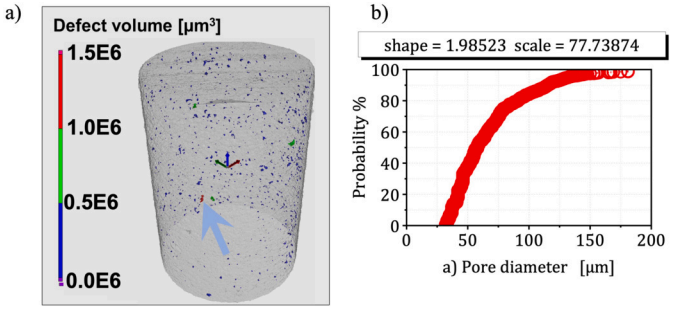


Fig. 11. Nondestructive testing of pore characteristics using X-ray microcomputed tomography of first standard exposure parameters identifying distributions of porosity according to Table 1: a) Three-dimensional render with critical defect; b) Weibull probability density graph.

Table 2
Cohesion energy and corresponding lattice parameters after application of DFT and the kinetic failure of solids.

Element	Cell	Atoms	$U_0(eV)$	$E(GPa)$	Vol.(A^{o3})	$a(A^o)$
Ti	HCP	2	-17.84	124	44.56	3.76

hysteresis loops are to be seen [32]. Their width and height change rapidly at the beginning of the test in a contracting fashion due to hardening until the behavior inflects into a softening phase characterized by increased softening due to large-scale granular plastic deformation and increased compliance of the specimen due to cracking. In high cycle fatigue, an intermediate saturation phase is observed where only microstructural cracking ensues and significant softening is yet to appear until the shift into long cracking. In very high cycle fatigue, the loads are away from the yield point, and the deformation mechanism is highly localized in the microstructure, which leads to negligible macroscopic observations. This is even exaggerated more while using ultrasonic fatigue testing devices due to high strain rate hardening [51]. The distinction between those regimes and identification of their load level boundaries is necessary for proper analysis modeling, prediction, and design for fatigue lifetimes. This distinction may have some grey areas depending on the complexity of the microstructure and secondary conditions, such as surface finish and residual defects. The continuous incremental load increase tests are high throughput techniques to estimate these load levels on the load spectrum. In Fig. 13, we represent the transition points (at which the derivative of the plastic strain amplitude curve is zero) of the fatigue loading spectrum of SLM Ti-6Al-4V based on the response of cyclic strain components of this test. From the plas-

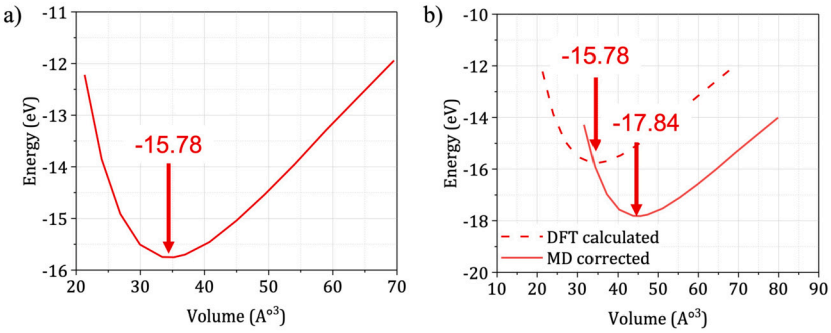


Fig. 12. Identification of cohesion energy of the microstructure of SLM Ti-6Al-4V: a) Theoretical result from DFT calculations; b) Result from molecular dynamics of the kinetic failure of solids.

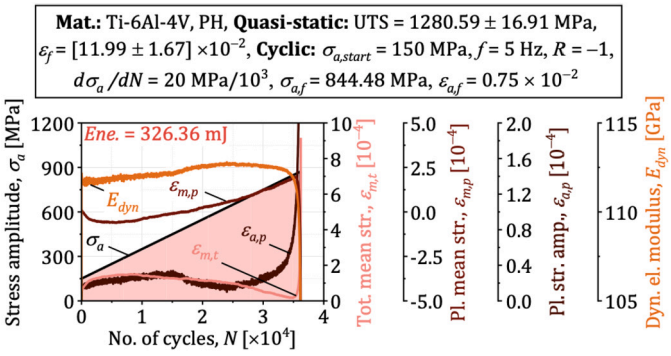


Fig. 13. Cyclic deformation under continuous incremental cyclic loading in the range of fatigue stress amplitudes; Energy × 1E2; Mat.: Material; PH: platform-heated; UTS: Ultimate tensile strength; ε_f: Fracture strain; $\sigma_{a,start}$: initial stress amplitude in LIT; f: frequency; R: stress ratio; $d\sigma_a/dN$: rate of increase of stress amplitude; $\sigma_{a,f}$: failure stress amplitude in LIT; $\varepsilon_{a,f}$: failure strain amplitude in LIT.

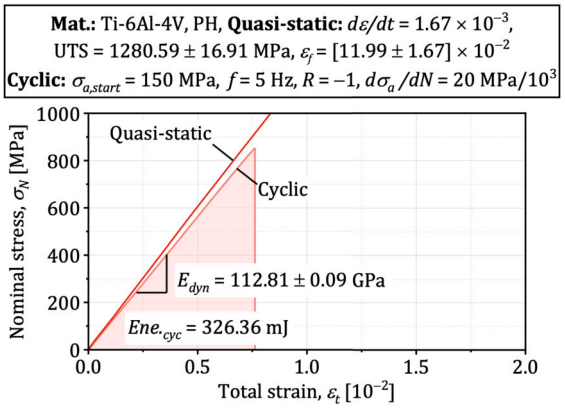


Fig. 14. Comparison between quasistatic and cyclic deformation characteristics in the range of fatigue loading; Energy × 1E2.

tic strain amplitude evolution, we can see a transition point at around 570 MPa into very high cycle fatigue. A transition occurs short of 800 MPa from low to high cycle fatigue.

In Fig. 14, the comparison between the quasi-static and low increase tests total strain relations hints at a decrease in elastic modulus and general softening of the microstructure due to the load reversals. The load reversals can constitute a basis for calibrating cyclic plasticity models, which can be used to compute the energy consumed per cycle and accurately capture the microstructure's saturation state. In Fig. 15, stepwise incremental loading is shown under displacement control to calibrate the isotropic part of the cyclic plasticity model. Every level provides a constitutive relation for the subsequent virtual constant amplitude

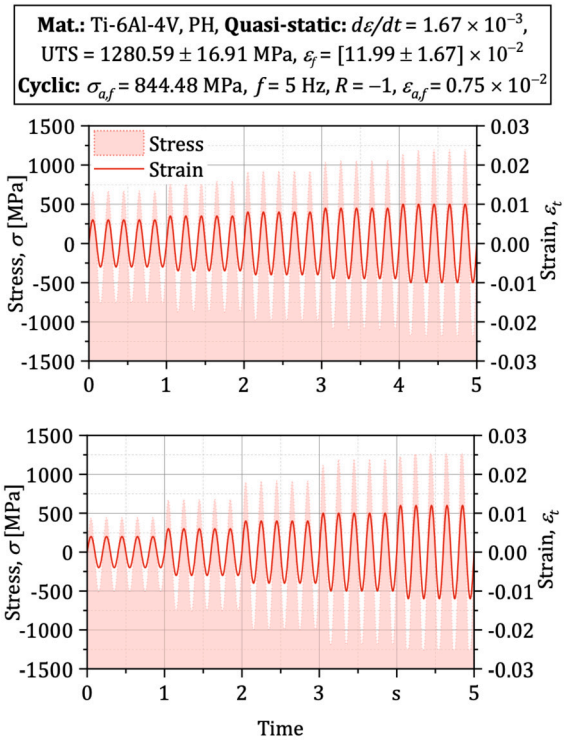


Fig. 15. Evolution of the yield locus to calculate damage due to plastic work by simulation of yield surface expansion.

test simulation. From this, the work done by the specimen is calculated, and the remaining lifetime can be tracked. The model in this configuration becomes simpler and does not consume prohibitive computational power in comparison to the fatigue damage model based on crystal plasticity, which needs significant computational power during model generation and load case simulation [78,15] or the need for numerically complex multi-scale homogenization of state variables across scales [79].

Establishment energy as a basis of modeling mechanics of fatigue also enables the adoption of fracture mechanics parameters from the same tests. Thus, calibration of a fracture mechanics model and a fatigue crack propagation simulation becomes possible within the same scheme without additional fracture toughness or fatigue crack propagation standardized test [80]. A crack propagation curve reveals the fatigue regime zones in great compliance with what was discussed in Fig. 13. Hence, a properly calibrated fatigue crack propagation simulation would reveal similar attributes. In addition to mechanism revelation, load level, and frequency dependencies can be visualized and compared. Fig. 16 shows such a comparison based on the simulation scheme of Fig. 8. We see a clear transition from microstructurally short

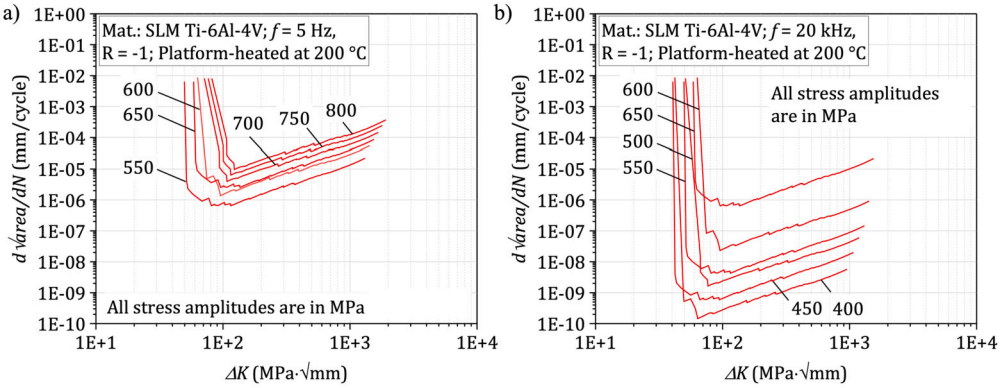


Fig. 16. Long and short fatigue crack propagation: a) Low-frequency simulations in high cycle fatigue; b) Ultrasonic frequency simulation in very high cycle fatigue; $d\sqrt{area}/dN$: rate of increase of area of crack with applied cycles; ΔK: cyclic stress intensity factor range.

to technically long crack propagation with a clear well of stress intensity factor that also characterizes the beginning of significant compliance of the specimen. We see also by steps of 50 MPa how the curves shift into the two o'clock direction. In the high-frequency simulation, the transition happens at much lower propagation rates but at similar stress intensity factor ranges. The whole set of curves appears to shift down with varying degrees. The corresponding shift to a 50 MPa step in the loading amplitude is significantly more significant. Details on the fatigue crack propagation simulation in this setup can be found in [48]. This is not the first attempt to simulate fatigue fracture using the extended finite element method [81–84,11]. However, it might be the first with an extensive degree of correlation to the manufacturing process and its induced flaws that are highly random.

3.4. Material energy losses

In the build-up of the model described here, we use energy as the base dimension and hence we represent the existence of defects inside fatigue specimens as loss of fatigue potential energy due to defects. Already internal surfaces have been formed in the defect formation process, which means that the energy released during the formation of these surfaces is not available anymore as potential energy inside the fatigue specimen to accommodate externally applied loads that result in internal damping, deformation, and potentially formation of fracture surfaces to release some of the stored energy. Fig. 17 represents the application of this concept where the experimental fatigue data of low-frequency tests, on servo-hydraulic machines, are shown. The figure shows two predicted blue points at 600 MPa of stress amplitude for the total life of the specimens. The blue star presents a prediction free of defects based on the DFT calculation and strength of the microstructure in Fig. 10b. The point already lies at the upper boundaries of the experimental data of specimens that carry almost no defects. The prediction at this point relies solely on the microstructure. No doubt that the experimental fatigue data present a trade-off between both influences of the microstructure and porosity since we tested polished specimens. However, in numerical modeling, as we see, the two factors can be separated. A prediction based on the same microstructural strength but with a total defect area of 1.385e5 μm^2 is shown in the blue hexagon. This point lies at the lower average value of life at this load level with almost an order of magnitude of fatigue strength reduction. Given this result, we can ultimately separate influences and predict the effects of defects given the same microstructure and vice versa in a very deterministic fashion relative to each other. The strength of the microstructure alone is calculated by the cohesion energy and is degraded by the amount of work the microstructure exerts per cycle until fracture. In section 2.4, the influence of defects is quantified separately and locally by calculating the energy required to form these defects from the surface energy of this alloy and removing this from the energy available

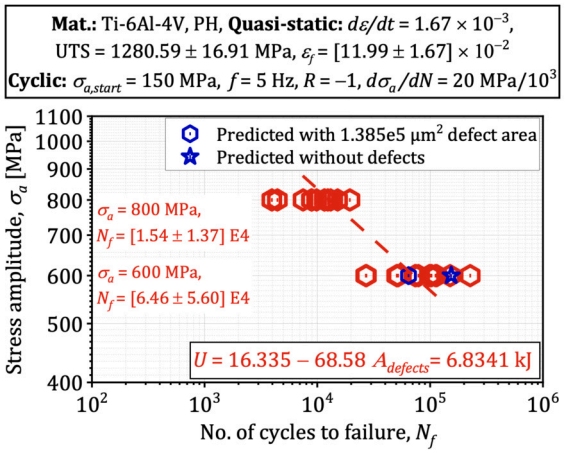


Fig. 17. The influence of potential energy loss on fatigue life under low-frequency testing for 1.385E5 μm^2 total defect area in SLM Ti-6Al-4V.

to the microstructure to accommodate the applied load. However, the variation of microstructural strength and defect formation location due to the thermal input become the primary source of uncertainty and the nature of probabilistic fatigue. Hence we further post-process the correlation between distributions of defects, microstructure, and process parameters using Bayesian statistics and Monte Carlo simulations.

It is worth mentioning that the model has good accountability of strain rate effects when testing at ultrasonic frequencies, such as in Fig. 18. The fatigue strength of the exact microstructural location is shown with a blue star since it is a prediction without porosity consideration. The effect of the same defect area 1.385e5 μm^2 is shown to its left by a blue hexagon where a half order of magnitude reduction could be seen in fatigue strength for the total life of the specimens. Combining both figures, the effect of strain rate can be distinguished in isolation from further effects which is an advantage of combining both numerical and experimental mechanics schemes. Crystal plasticity models directly considered based on representative volume elements (RVE) focus on the variability of the microstructure and trade the property variability for the statistical representation of the microstructure [85,86,7,87–90]. It renders the correlation process parameter variability to property variability easier if a multitude of RVEs is virtually tested, which adds up the computational cost of the modeling process.

3.5. Physics-informed machine learning

The Γ distributions have been used extensively to describe and predict failure rate problems [53]. The weakest links model based on the Weibull distribution was extensively used in fatigue literature to describe scatter in fatigue data [19,21,91–95,23,22,20]. These literatures

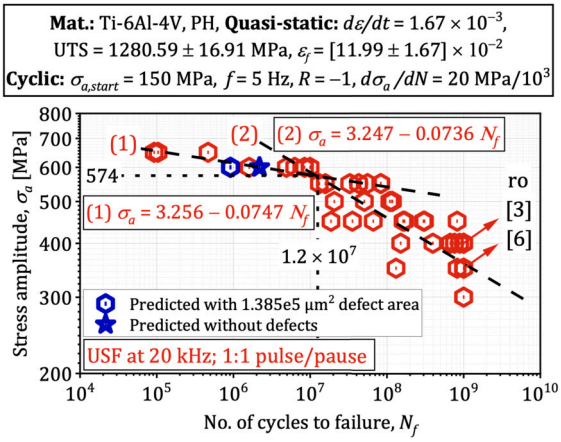


Fig. 18. The influence of potential energy loss on fatigue life under high-frequency testing for 1.385E5 µm² total defect area in SLM Ti-6Al-4V.

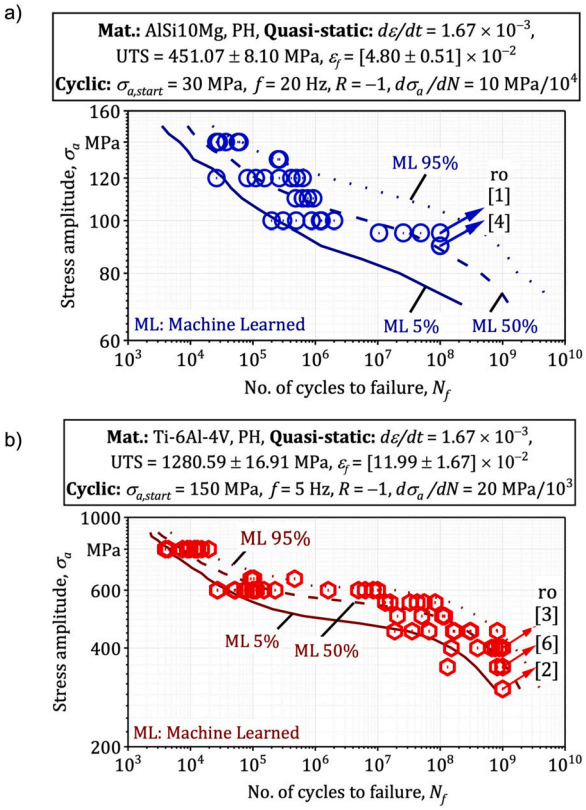


Fig. 19. Validation of the probabilistic regression model that forms the elementary activation function of the machine learning model on SLM: a) AlSi10Mg; b) Ti-6Al-4V.

describe a varying aspect of the fatigue damage problem with varying success based on the scheme in which they are integrated. In this study, we used plasticity parameter optimizations based on the instrumented indentations in which the optimization starts at the trivial cohesion energy coming out of the first principle calculations. These physically modeled predictions have been used during the training phase of the model. Experimental data from the fatigue tests have been used to validate the predictions of the machine learning models. Hence, there was no data splitting of the same group for training and testing; on the contrary, the training and testing data come from independent roots. The dispersion of fatigue data is accounted for in this multilayer learning by the probabilistic regression and uncertainty analysis within the Γ probability density function. The deterministic validity of the model that can isolate microstructure and defect influences have been shown in Figs. 17 and 18. We have solved numerous scenarios such as these, starting from the cohesion energy of the first principles under the variability of the microstructures indented and defects identified from µ-CT scans. Hence, we were able to establish the probabilistic regression activation functions of the network and, with them, fit $S-N$ curve percentiles from low cycle to very high cycle fatigue with varying asymptotes and dynamic biases in the extension of the work by [49] which was accurate only locally in the high cycle fatigue regime based on the biases of available experimental data. However, due to the efficiency of the represented model in this study, data can be provided as needed in terms of quantity and quality of variability until saturation or precision is achieved. The performance of the implemented Weibull regression is compared to experimental data in Fig. 19 for two popular additive manufacturing alloys AlSi10Mg and Ti-6Al-4V. The prediction and validation represent the total life of the specimens.

The saturation of precision is presented in Fig. 20 during the reinforcement learning algorithm, which relies on the Metropolis Monte Carlo scheme. The saturation process optimizes the characteristic parameters of the Weibull and Gumbel regression models such that the resulting parameters become more presentable of the population of the parameter of interest. Fig. 20a shows 100 withdrawals from the density function of the porosity. The process has a random footprint. However, in Fig. 20b, we overwrite the current parameters if we encounter a withdrawal that has a higher probability, thus reinforcing the new parameters on the old ones in preparation for the Weibull regression scheme where the percentiles get tuned to the $S-N$ relationship identified by the mechanistic function. Reinforcement learning has been used since the 1990s to solve linear systems of equations by coupling what the authors call unorthodox Monte Carlo methods [96]. They proved that for large-scale problems, the reinforcement learning technique has an efficiency advantage. The current study's authors agree with this and show that fatigue as a highly random, physically complex problem can be solved using reinforcement learning algorithms. Abbeel and Ng [97] used criteria to maximize an expressible reward function as a linear combination of known features, and give an algorithm for learning the task, such as fatigue damage demonstrated by the mechanistic function. Hence, in the current study, we inverse the reinforcement learning process by extracting the most likely expected outcome given an optimal result provided by a mechanistic function such as what is shown by Ng and Russell [18].

Monte Carlo simulations are well suited to solve the fatigue problem because it has a lot of combinatorial factors related to complicated interconnected damage mechanisms. Therefore they describe the influence of stochastic structural features on net fatigue properties. To remain within efficient computational boundaries on the main aims of this study, we need to determine if our Markov chain has been running long enough to be stable enough to equilibrium. The irreducibility of the finite discrete-time Markov chain leads to an exponential convergence to the equilibrium. The spectral gap identifies the engine values much better in comparison to the constants of the theory, as shown in Fig. 21a. Until a stationary distribution of the feature is reached and its transition matrix becomes irreducible, the fatigue process based on the Γ distribution jumps from a damaged state to a damaged state based on the transition matrix as shown in Fig. 21b. These transition probabilities of features can be isolated, combined, or handled by Bayes' rule. The presentation of the wide spectral gap is proportional to the exponential conversion of the chain as proof that Markov sampling from this probity distribution has been stable enough. We repeat these processes for microstructure in addition to the shown spectral gap and transition probability of porosity. We also combine all available measurands of energy input like temperature, microstructure, and porosity to produce fatigue design maps based on this metadata in a Bayesian model. In Fig. 22, we show two maps representing influences of heat energy input based on porosity and microstructure variability, respectively. The

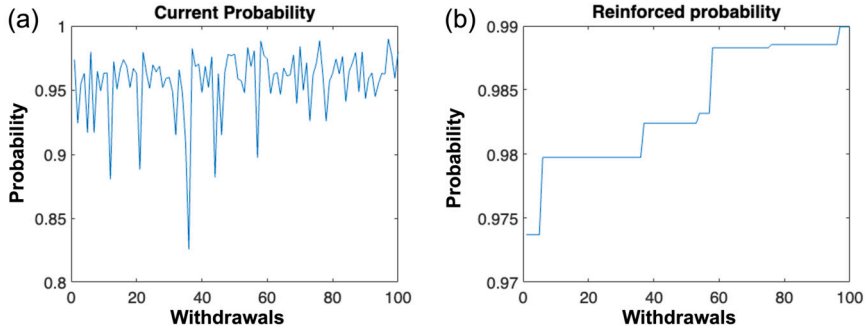


Fig. 20. Progression of Γ parameters by comparison between a) Current probability and b) Reinforced probability.

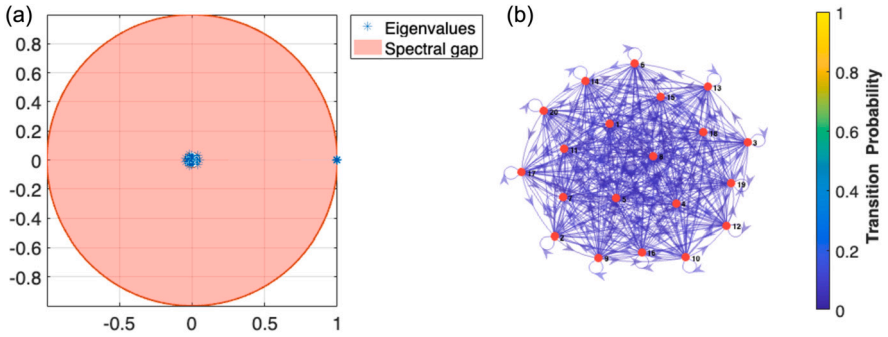


Fig. 21. Visualization of Markov chain of the porosity of Ti-6Al-4V: a) Eigenvalues and b) Transition probability.

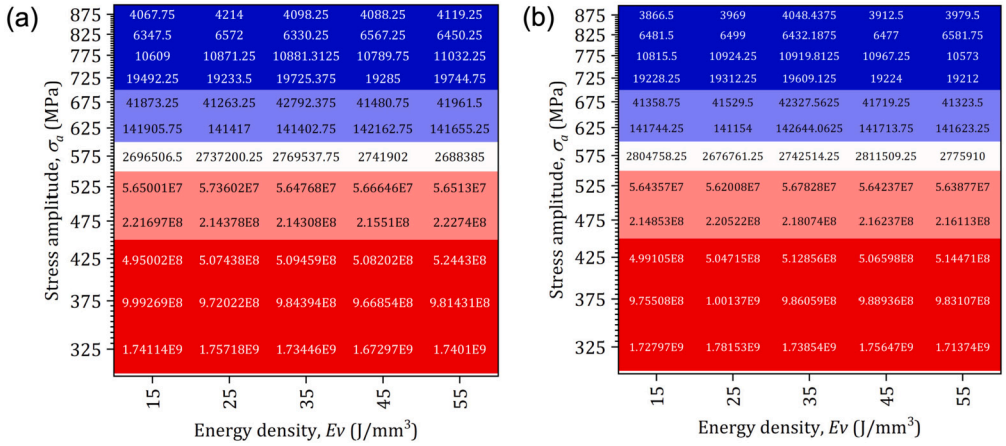


Fig. 22. Fatigue lifetime property map based on the metadata of phenomenological modeling and machine learning process concerning the variability of: a) Porosity and b) Microstructure; (Lifetime in cycles).

maps and their extension of the complete data set enable optimized design against fatigue damage using the metadata before processing and accelerate the process qualification lead time to serial production. Additionally, with high throughput measurement techniques, manufacturing faults can be detected online and corrected from information provided by the heat map.

4. Conclusions and outlook

In this article, probabilistic regression has been coupled with reinforcement learning to achieve nonlinear regression of additive manufacturing processes' physical parameters with fatigue strength. For the first time:

1. The fatigue design process could start before processing through mechanistic machine learning and the coupling of deep neural layers of diverse regression schemes with numerical techniques of high dimensional integrals that highly embrace multi-scale multi-physics.
2. The introduced machine learning methodology is effective in a specific predetermined process window corresponding to the problem's boundary conditions.
3. More control can be achieved over properties by targeting strictly quantitative process-property conjugates and higher production efficiency in using energy and materials.
4. Fatigue-damage tolerant materials can be designed in advance to actual production based on the historical metadata of the production processes and the in-service damage characteristics.
5. By applying a machine learning model on a mechanistic function that represents the physics of the fatigue problem within specific boundary conditions, fatigue-resistant designs can be introduced in the process development phase.
6. If the physical boundary conditions are to be changed, the mechanistic model can be used to generate training data for the machine

learning model with a physical boundary space, enabling fatigue lifetime predictions to be made computationally efficient without explicitly solving the physics behind it.
7. The authors advise the reader to focus on the idea that the machine learning model remains valid within its trained physical space provided by the mechanistic function.
8. Property control of Ti-6Al-4V in a selective laser melting machine can be realized with various second exposure treatments.
9. The effect of secondary exposure on fatigue strength induced by microstructural modification has been quantitatively estimated.
10. The current standard experimental qualification is expensive when it has to cope with the flexibility of modern manufacturing processes.
11. State-of-the-art numerical techniques alone are not computational or time-efficient.
12. Combining local instrumented indentation testing to calibrate mechanistic functions that get the best first-guess solutions from density functional theory can increase the efficiency of testing procedures.
13. Generation of artificial outcomes as training data for the machine learning model in the calibrated physical space can make online predictions and provide feedback.
14. The control of metadata of the manufacturing process enables fatigue meta designs that were impossible to obtain previously.
15. Meta designs of materials contain sub-ensembles of material that perform specific functions like crack retardation or deflection from critically loaded areas.
16. The meta-design has metadata of the structure and can recall it whenever the user defines new desired attributes or the process encounters any malfunction, such as a fall of expectation of specific fatigue damage tolerances.

In the following study, we will introduce the concept of cyber-physical additive manufacturing systems based on mechanistic machine learning concepts:

1. This concept will mark a transformative phase in manufacturing because it will seamlessly blend the digital and physical realms to enhance the efficiency and capabilities of digital manufacturing.
2. This interconnected system facilitates real-time data exchange, predictive analytics, and advanced automation, collectively steering traditional manufacturing into a new era of enhanced capabilities and efficiency.
3. Currently, the landscape of cyber-physical AM is at a critical juncture, where the integration of advanced technologies aims to transform traditional manufacturing processes digitally.
4. The overarching objective is to optimize and streamline the entire AM workflow through intelligent connectivity.

CRediT authorship contribution statement

Mustafa Awd: Writing – original draft, Visualization, Software, Methodology, Investigation, Conceptualization. **Lobna Saeed:** Writing – review & editing, Writing – original draft, Software, Methodology, Investigation, Data curation, Conceptualization. **Sebastian Münstermann:** Writing – review & editing, Visualization, Supervision, Methodology. **Matthias Faes:** Writing – review & editing, Supervision. **Frank Walther:** Writing – review & editing, Project administration, Funding acquisition.

Declaration of competing interest

The authors declare the following financial interests/personal relationships which may be considered as potential competing interests: Prof. Frank Walther reports financial support was provided by German Research Foundation. If there are other authors, they declare that they have no known competing financial interests or personal relationships that could have appeared to influence the work reported in this paper.

Data availability

The data that has been used is confidential.

Acknowledgements

The authors thank the German Research Foundation (Deutsche Forschungsgemeinschaft, DFG) for its financial support within the research project “Mechanism-based understanding of functional grading focused on fatigue behavior of additively processed Ti-6Al-4V and Al-12Si alloys” (WA 336368661). The authors further thank Fraunhofer IAPT, Hamburg, for providing the specimens and thermal measurements in the framework of excellent scientific collaboration.

Appendix A. Introduction to density functional theory

The Born-Oppenheimer approximation reduces the time-independent anti-relativistic SE of a multi-body problem to [98]

$$\left[\frac{-\hbar^2}{2m}\sum_{i=1}^{N}\nabla_i^2+\sum_{i=1}^{N}V(\mathbf{r_i})+\sum_{i=1}^{N}\sum_{j<1}U(\mathbf{r_i},\mathbf{r_j})\right]\Psi=E\Psi \tag{57}$$

with m and N being the mass of the electron and the number of electrons, respectively. E is the electrons' ground-state energy, and $\Psi=\Psi(r_1,...,r_N)$. The Hartree-Fock approximation applies the Slater determinant to account for the antisymmetry of the wave function or, in other words, to prevent two electrons of the same spin from being situated at the same point in space [99]

$$\left[\frac{-\hbar^2}{2m}\nabla_i^2+V_{ion}(x_i)+V_i^H+V_i^x\right]\Psi=E\Psi \tag{58}$$

The Hartree-Fock method failed to consider the electronic correlation due to Coulomb interaction; solving this many-body SE even with post-Hartree-Fock methods, is very expensive and sometimes not computationally tractable. DFT is an exact reformulation of quantum mechanics based on two theorems: first, the ground state energy can uniquely determine the ground state properties; hence, the ground state energy is functional of the density function $n(r)$. Second, the actual electron density corresponding to the ground state energy is the density that minimizes the energy of the global functional. The energy functional can be written as [100]

$$E[\Psi]=E_{known}[\Psi]+E_{XC}[\Psi] \tag{59}$$

where the E_{known} is [101]

$$E_{known}[\Psi]=\frac{-\hbar^2}{m}\sum_i\int\Psi_i^*\nabla^2\Psi_i\,d^3r+\int V(\mathbf{r})\,n(\mathbf{r})\,d^3r+\frac{e^2}{r}\int\int\frac{n(\mathbf{r})n'(\mathbf{r}')}{|(\mathbf{r})-(\mathbf{r}')|}\,d^3r\,d^3r'+E_{ion} \tag{60}$$

with the first term, in order, is the kinetic energy of the electron, the second term is the electrons-nuclei interaction, the third term is the electron-electron interaction, and, finally, the last one is the nuclei interaction due to Coulomb potential. The second term, E_{XC}, is the exchange-correlation functional containing all quantum mechanical effects not included in the E_{known} term. Finding this E_{XC} functional is not easier than solving the many-body SE. KS reformulated this to express each equation with a single electron. The single particles KS equation can be written as [100]

$$\left[\frac{-\hbar^2}{2m}\nabla_i^2+V(\mathbf{r})+V_H(\mathbf{r})+V_{XC}(\mathbf{r})\right]\Psi_i(\mathbf{r})=\epsilon_i\Psi_i(\mathbf{r}) \tag{61}$$

with V is the potential that appeared in equation (57), the Hartree potential V_H is [102]

$$V_H(\mathbf{r}) = e^2 \int \frac{n(\mathbf{r}')}{|\mathbf{r}-\mathbf{r}'|}\, d^3r' \tag{62}$$

and finally the exchange-correlation potential V_{XC} which is the derivative of the exchange-correlation energy functional is [103]

$$V_{XC}(\mathbf{r}) = \frac{\delta E_{XC}(\mathbf{r})}{\delta(\mathbf{r})} \tag{63}$$

Before solving E_{XC} functional, DFT can not be used in practical applications. This method handles the exchange-correlation effects within the generalized gradient approximation (GGA) using the Perdew-Burke-Ernzerhof (PBE) formulation. The Vienna ab initio simulation package (VASP) was employed using the projector augmented wave (PAW) potential method [104] where the new charge density after going through the self-consistent loop is

$$n_{KS}(\mathbf{r}) = 2\sum_i \Psi_i^*(\mathbf{r})\Psi_i(\mathbf{r}) \tag{64}$$

and the exchange-correlation potential V_{XC}^{GGA} is

$$V_{XC}^{GGA}(\mathbf{r}) = V_{XC}[n(\mathbf{r}), \nabla(n(\mathbf{r}))] \tag{65}$$

References

[1] Q. Pan, L. Jing, L. Lu, Enhanced fatigue endurance limit of cu through low-angle dislocation boundary, 244 118542, https://doi.org/10.1016/j.actamat.2022.118542, https://www.sciencedirect.com/science/article/pii/S1359645422009193.

[2] H.S. Queiroz, J.A. Araújo, C.R.M. Silva, J.L.A. Ferreira, A coupled critical plane-area methodology to estimate fatigue life for an AISI 1045 steel with small artificial defects, 121 103426, https://doi.org/10.1016/j.tafmec.2022.103426, https://www.sciencedirect.com/science/article/pii/S0167844222001732.

[3] C. Zhang, W. Lu, Unveiling contribution of overload-induced residual stress to fatigue retardation pertinent to crack closure and stress intensity, 831 142268, https://doi.org/10.1016/j.msea.2021.142268, https://www.sciencedirect.com/science/article/pii/S092150932101532X.

[4] E. Salvati, H. Zhang, K.S. Fong, X. Song, A.M. Korsunsky, Separating plasticity-induced closure and residual stress contributions to fatigue crack retardation following an overload, 98 222–235, https://doi.org/10.1016/j.jmps.2016.10.001, https://www.sciencedirect.com/science/article/pii/S0022509616305531.

[5] A. Zafra, G. Álvarez, G. Benoit, G. Henaff, E. Martinez-Pañeda, C. Rodríguez, J. Belzunce, Hydrogen-assisted fatigue crack growth: pre-charging vs in-situ testing in gaseous environments, 144885, https://doi.org/10.1016/j.msea.2023.144885, https://linkinghub.elsevier.com/retrieve/pii/S092150932300309X.

[6] E. Maleki, S. Bagherifard, M. Guagliano, Correlation of residual stress, hardness and surface roughness with crack initiation and fatigue strength of surface treated additive manufactured AlSi10mg: experimental and machine learning approaches, 24 3265–3283, https://doi.org/10.1016/j.jmrt.2023.03.193, https://www.sciencedirect.com/science/article/pii/S2238785423006555.

[7] S. Lucarini, F. Dunne, E. Martínez-Pañeda, An FFT-based crystal plasticity phase-field model for micromechanical fatigue cracking based on the stored energy density, 172 107670, https://doi.org/10.1016/j.ijfatigue.2023.107670, https://linkinghub.elsevier.com/retrieve/pii/S0142112323001718.

[8] E. Salvati, S. O'Connor, T. Sui, D. Nowell, A.M. Korsunsky, A study of overload effect on fatigue crack propagation using EBSD, FIB–DIC and FEM methods, 167 210–223, https://doi.org/10.1016/j.engfracmech.2016.04.034, https://www.sciencedirect.com/science/article/pii/S0013794416301990.

[9] M. Jones, B. Main, K. Maxfield, S. Barter, R. Das, Predicting fatigue crack growth through the small and long crack regimes for a military transport aircraft loading spectrum using FASTRAN, 171 107576, https://doi.org/10.1016/j.ijfatigue.2023.107576, https://www.sciencedirect.com/science/article/pii/S0142112323000774.

[10] M. Awd, F. Walther, Machine learning of fatigue strength of hybrid and additively manufactured aluminum alloys in VHCF regime, West Conshohocken, PA: ASTM International 262–276, https://doi.org/10.1520/STP164320210096.

[11] Z. Cheng, H. Wang, G.-R. Liu, Fatigue crack propagation in carbon steel using RVE based model, 258 108050, https://doi.org/10.1016/j.engfracmech.2021.108050, https://www.sciencedirect.com/science/article/pii/S0013794421004677.

[12] K.J. Dogahe, I. Kurz, P. Binkele, S. Schmauder, M. Mlikota, Z. Bozic, Physically-based modelling of the fatigue crack initiation life of stent components under cyclic loading employing the finite-element-method (fem), 171 107594, https://doi.org/10.1016/j.ijfatigue.2023.107594, https://www.sciencedirect.com/science/article/pii/S0142112323000956.

[13] H.W. Lee, C. Basaran, H. Egner, A. Lipski, M. Piotrowski, S. Mroziński, N. Bin Jamal M, C. Lakshmana Rao, Modeling ultrasonic vibration fatigue with unified mechanics theory, 236-237 111313, https://doi.org/10.1016/j.ijsolstr.2021.111313, https://www.sciencedirect.com/science/article/pii/S0020768321003930.

[14] K. Tang, K. Chen, P. Ferro, F. Berto, Quantifying lamellar microstructural effect on the fatigue performance of bimodal ti-6al-4v with microdefect, 163 107045, https://doi.org/10.1016/j.ijfatigue.2022.107045, https://www.sciencedirect.com/science/article/pii/S0142112322003103.

[15] K.-S. Li, R.-Z. Wang, G.-J. Yuan, S.-P. Zhu, X.-C. Zhang, S.-T. Tu, H. Miura, A crystal plasticity-based approach for creep-fatigue life prediction and damage evaluation in a nickel-based superalloy, 143 106031, https://doi.org/10.1016/j.ijfatigue.2020.106031, https://www.sciencedirect.com/science/article/pii/S0142112320305636.

[16] A. Ciampaglia, A. Tridello, D. Paolino, F. Berto, Data driven method for predicting the effect of process parameters on the fatigue response of additive manufactured AlSi10mg parts, 170 107500, https://doi.org/10.1016/j.ijfatigue.2023.107500, https://linkinghub.elsevier.com/retrieve/pii/S0142112323000014.

[17] P. White, Molecular dynamic modelling of fatigue crack growth in aluminium using LEFM boundary conditions, 44 141–150, https://doi.org/10.1016/j.ijfatigue.2012.05.005, https://www.sciencedirect.com/science/article/pii/S0142112312001764.

[18] A.Y. Ng, S. Russell, Algorithms for inverse reinforcement learning, in: Icml, vol. 1, p. 2.

[19] A. Wormsen, B. Sjödin, G. Härkegård, A. Fjeldstad, Non-local stress approach for fatigue assessment based on weakest-link theory and statistics of extremes, 30 (12) 1214–1227, https://doi.org/10.1111/j.1460-2695.2007.01190.x, https://onlinelibrary.wiley.com/doi/10.1111/j.1460-2695.2007.01190.x.

[20] P. Baldissera, C. Delprete, The formal analogy between Tanaka-Mura and Weibull models for high-cycle fatigue: fatigue micro-mechanical models analogy, 35 (2) 114–121, https://doi.org/10.1111/j.1460-2695.2011.01598.x, https://onlinelibrary.wiley.com/doi/10.1111/j.1460-2695.2011.01598.x.

[21] E. Castillo, A. Ramos, R. Koller, M. López-Aenlle, A. Fernández-Canteli, A critical comparison of two models for assessment of fatigue data, 30 (1) 45–57, https://doi.org/10.1016/j.ijfatigue.2007.02.014, https://linkinghub.elsevier.com/retrieve/pii/S0142112307000679.

[22] A. Fernández-Canteli, C. Przybilla, M. Nogal, M.L. Aenlle, E. Castillo, Profatigue: a software program for probabilistic assessment of experimental fatigue data sets, 74 236–241, https://doi.org/10.1016/j.proeng.2014.06.255, https://linkinghub.elsevier.com/retrieve/pii/S187770581400825X.

[23] J. Gao, Y. Yuan, Probabilistic model of fatigue damage accumulation of materials based on the principle of failure probability equivalence, 28 659–667, https://doi.org/10.1016/j.istruc.2020.09.023, https://www.sciencedirect.com/science/article/pii/S2352012420304999.

[24] M. Awd, Machine learning algorithm for fatigue fields in additive manufacturing, reports of materials science and engineering, Springer Fachmedien, Wiesbaden, https://doi.org/10.1007/978-3-658-40237-2, https://link.springer.com/10.1007/978-3-658-40237-2.

[25] J.R. Chelikowsky, Introductory Quantum Mechanics with MATLAB: for Atoms, Molecules, Clusters, and Nanocrystals, John Wiley & Sons, google-Books-ID, QRVqDwAAQBAJ.

[26] Dynamical systems in applications, Łódź. Poland December 11–14, 2017, https://doi.org/10.1007/978-3-319-96601-4, http://link.springer.com/10.1007/978-3-319-96601-4.

[27] N.G. Stephen, On energy harvesting from ambient vibration, 293 (1) 409–425, https://doi.org/10.1016/j.jsv.2005.10.003, https://www.sciencedirect.com/science/article/pii/S0022460X05006784.

[28] L.J. Rodríguez-Aragón, J. López-Fidalgo, Optimal designs for the Arrhenius equation, 77 (1) 131–138, https://doi.org/10.1016/j.chemolab.2004.06.007, https://www.sciencedirect.com/science/article/pii/S0169743904001753.

[29] Z. Yang, K.N. Houk, The dynamics of chemical reactions: atomistic visualizations of organic reactions, and homage to van 't Hoff, 24 (16) 3916–3924, _eprint: https://onlinelibrary.wiley.com/doi/pdf/10.1002/chem.201706032, https://onlinelibrary.wiley.com/doi/abs/10.1002/chem.201706032.

[30] M.J. Mehl, D. Hicks, C. Toher, O. Levy, R.M. Hanson, G. Hart, S. Curtarolo, The AFLOW library of crystallographic prototypes: part 1, 136 S1–S828, https://doi.org/10.1016/j.commatsci.2017.01.017, https://www.sciencedirect.com/science/article/pii/S0927025617300241.

[31] J. Stewart, Calculus, 7th Edition, Brooks/Cole, Cengage Learning, OCLC, ocn651906312.

[32] F. Ellyin, Fatigue damage, crack growth and life prediction, Springer, OCLC, 801662192.

[33] J.L. Hay, G.M. Pharr, Instrumented indentation testing 8 10.

[34] W. Oliver, G. Pharr, An improved technique for determining hardness and elastic modulus using load and displacement sensing indentation experiments, 7 (6) 1564–1583, https://doi.org/10.1557/JMR.1992.1564, http://link.springer.com/10.1557/JMR.1992.1564.

[35] R.T. DeHoff, Thermodynamics in materials science, OCLC: 1052119396, https://nls.ldls.org.uk/welcome.html?ark:/81055/vdc_100046146163.0x000001.

[36] D. Wang, L.-S. Fan, Particle characterization and behavior relevant to fluidized bed combustion and gasification systems, in: Fluidized Bed Technologies for Near-Zero Emission Combustion and Gasification, Elsevier, pp. 42–76, https://doi.org/10.1533/9780857098801.1.42, https://linkinghub.elsevier.com/retrieve/pii/B9780857095411500029.
[37] V.A. Svetlitsky, Statics of rods, foundations of engineering mechanics, Springer Berlin Heidelberg, https://doi.org/10.1007/978-3-540-45593-6, http://link.springer.com/10.1007/978-3-540-45593-6.
[38] M. Awd, M.F. Labanie, K. Moehring, A. Fatemi, F. Walther, Towards deterministic computation of internal stresses in additively manufactured materials under fatigue loading: part I, 13 (10) 2318, https://doi.org/10.3390/ma13102318, https://www.mdpi.com/1996-1944/13/10/2318.
[39] K. Zhao, J. Lee, Finite element analysis of the three-point bending of sheet metals, 122 (1) 6–11, https://doi.org/10.1016/S0924-0136(01)01064-0, https://linkinghub.elsevier.com/retrieve/pii/S0924013601010640.
[40] A. Fatemi, D.F. Socie, A critical plane approach to multiaxial fatigue damage including out-of-phase loading, 11 (3) 149–165, https://doi.org/10.1111/j.1460-2695.1988.tb01169.x, http://doi.wiley.com/10.1111/j.1460-2695.1988.tb01169.x.
[41] N.R. Gates, A. Fatemi, On the consideration of normal and shear stress interaction in multiaxial fatigue damage analysis, 100 322–336, https://doi.org/10.1016/j.ijfatigue.2017.03.042, https://linkinghub.elsevier.com/retrieve/pii/S0142112317301603.
[42] S.N. Zhurkov, Kinetic concept of the strength of solids, 1 (4) 311–323, https://doi.org/10.1007/BF03545562, https://link.springer.com/10.1007/BF03545562.
[43] S.-W. Jeon, K.-W. Lee, J.Y. Kim, W.J. Kim, C.-P. Park, D. Kwon, Estimation of fracture toughness of metallic materials using instrumented indentation: critical indentation stress and strain model, 57 (7) 1013–1025, https://doi.org/10.1007/s11340-016-0226-2, http://link.springer.com/10.1007/s11340-016-0226-2.
[44] H.-K. Oh, Determination of fracture toughness by uniaxial tensile test, 55 (5) 865–868, https://doi.org/10.1016/0013-7944(96)00238-X, https://linkinghub.elsevier.com/retrieve/pii/001379449600238X.
[45] M. Janssen, J. Zuidema, R.J.H. Wanhill, Fracture mechanics, 2nd Edition, Spon Press, OCLC, ocm54778455.
[46] E.E. Gdoutos, Fracture mechanics, Solid Mechanics and Its Applications, vol. 14, Springer, Netherlands, https://doi.org/10.1007/978-94-015-8158-5, http://link.springer.com/10.1007/978-94-015-8158-5.
[47] T. Belytschko, T. Black, Elastic crack growth in finite elements with minimal remeshing, 45 (5) 601–620, https://doi.org/10.1002/(SICI)1097-0207(19990620)45:5<601::AID-NME598>3.0.CO, 2-S;
https://onlinelibrary.wiley.com/doi/abs/10.1002/%28SICI%291097-0207%2819990620%2945%3A5%3C601%3A%3AAID-NME598%3E3.0.CO%3B2-S.
[48] M. Awd, F. Walther, Numerical investigation of the influence of fatigue testing frequency on the fracture and crack propagation rate of additive-manufactured AlSi10mg and ti-6al-4v alloys, 3 (3) 430–446, https://doi.org/10.3390/solids3030030, https://www.mdpi.com/2673-6497/3/3/30.
[49] E. Castillo, A. Fernández-Canteli, a unified statistical methodology for modeling fatigue damage, Springer, OCLC, ocn253227766.
[50] E. Castillo, J. Galambos, J.M. Sarabia, The selection of the domain of attraction of an extreme value distribution from a set of data, in: J. Hüsler, R.-D. Reiss (Eds.), Extreme Value Theory, in: series Title: Lecture Notes in Statistics, vol. 51, Springer, New York, pp. 181–190, https://doi.org/10.1007/978-1-4612-3634-4_16, http://link.springer.com/10.1007/978-1-4612-3634-4_16.
[51] B. Pyttel, D. Schwerdt, C. Berger, Very high cycle fatigue – is there a fatigue limit?, 33 (1) 49–58, https://doi.org/10.1016/j.ijfatigue.2010.05.009, https://linkinghub.elsevier.com/retrieve/pii/S0142112310001362.
[52] M. Awd, S. Münstermann, F. Walther, Effect of microstructural heterogeneity on fatigue strength predicted by reinforcement machine learning, 45 (11) 3267–3287, https://doi.org/10.1111/ffe.13816, https://onlinelibrary.wiley.com/doi/10.1111/ffe.13816.
[53] R.E. Walpole, R.H. Myers, S.L. Myers, K. Ye, Probability & statistics for engineers & scientists: MyStatLab update, OCLC: 1014366070, http://www.myilibrary.com?id=947904.
[54] G.B. Dantzig, Maximization of a linear function of variables subject to linear, inequalities 13, 339–347.
[55] H. Nabli, An overview on the simplex algorithm, 210 (2) 479–489, https://doi.org/10.1016/j.amc.2009.01.013, https://www.sciencedirect.com/science/article/pii/S0096300309000198.
[56] T. Vilaro, C. Colin, J.D. Bartout, As-fabricated and heat-treated microstructures of the ti-6al-4v alloy processed by selective laser melting, 42 (10) 3190–3199, https://doi.org/10.1007/s11661-011-0731-y, http://link.springer.com/10.1007/s11661-011-0731-y.
[57] M. Simonelli, Y.Y. Tse, C. Tuck, On the texture formation of selective laser melted ti-6al-4v, 45 (6) 2863–2872, https://doi.org/10.1007/s11661-014-2218-0, http://link.springer.com/10.1007/s11661-014-2218-0.
[58] S.S. Al-Bermani, M.L. Blackmore, W. Zhang, I. Todd, The origin of microstructural diversity, texture, and mechanical properties in electron beam melted ti-6al-4v, 41 (13) 3422–3434, https://doi.org/10.1007/s11661-010-0397-x, http://link.springer.com/10.1007/s11661-010-0397-x.
[59] B. Vrancken, L. Thijs, J.-P. Kruth, J. Van Humbeeck, Heat treatment of ti-6al-4v produced by selective laser melting: microstructure and mechanical properties, 541 177–185, https://doi.org/10.1016/j.jallcom.2012.07.022, https://linkinghub.elsevier.com/retrieve/pii/S0925838812011826.
[60] T.A. Book, M.D. Sangid, Strain localization in ti-6al-4v widmanstätten microstructures produced by additive manufacturing, 122 104–112, https://doi.org/10.1016/j.matchar.2016.10.018, https://linkinghub.elsevier.com/retrieve/pii/S1044580316306167.
[61] Z. Zou, M. Simonelli, J. Katrib, G. Dimitrakis, R. Hague, Microstructure and tensile properties of additive manufactured ti-6al-4v with refined prior-beta grain structure obtained by rapid heat treatment, 814 141271, https://doi.org/10.1016/j.msea.2021.141271, https://linkinghub.elsevier.com/retrieve/pii/S0921509321005402.
[62] S. Beretta, S. Romano, A comparison of fatigue strength sensitivity to defects for materials manufactured by AM or traditional processes, 94 178–191, https://doi.org/10.1016/j.ijfatigue.2016.06.020, https://linkinghub.elsevier.com/retrieve/pii/S0142112316301645.
[63] M. Hamidi Nasab, M. Vedani, R.E. Logé, N. Sohrabi, A.M. Jamili, A. du Plessis, S. Beretta, An investigation on the fatigue behavior of additively manufactured laser shock peened AlSi7mg alloy surfaces, 200 112907, https://doi.org/10.1016/j.matchar.2023.112907, https://www.sciencedirect.com/science/article/pii/S1044580323002656.
[64] F. Sausto, C. Tezzele, S. Beretta, Analysis of fatigue strength of l-PBF AlSi10mg with different surface post-processes: effect of residual stresses, 12 (6) 898, number: 6 Publisher: Multidisciplinary Digital Publishing Institute, https://doi.org/10.3390/met12060898, https://www.mdpi.com/2075-4701/12/6/898.
[65] U. Zerbst, G. Bruno, J.-Y. Buffière, T. Wegener, T. Niendorf, T. Wu, X. Zhang, N. Kashaev, G. Meneghetti, N. Hrabe, M. Madia, T. Werner, K. Hilgenberg, M. Koukolíková, R. Procházka, J. Džugan, B. Möller, S. Beretta, A. Evans, R. Wagener, K. Schnabel, Damage tolerant design of additively manufactured metallic components subjected to cyclic loading: state of the art and challenges, 121 100786, https://doi.org/10.1016/j.pmatsci.2021.100786, https://linkinghub.elsevier.com/retrieve/pii/S0079642521000104.
[66] S. Siddique, M. Imran, M. Rauer, M. Kaloudis, E. Wycisk, C. Emmelmann, F. Walther, Computed tomography for characterization of fatigue performance of selective laser melted parts, 83 661–669, https://doi.org/10.1016/j.matdes.2015.06.063, https://linkinghub.elsevier.com/retrieve/pii/S026412751500413X.
[67] S. Siddique, M. Awd, J. Tenkamp, F. Walther, Development of a stochastic approach for fatigue life prediction of AlSi12 alloy processed by selective laser melting, 79 34–50, https://doi.org/10.1016/j.engfailanal.2017.03.015, https://linkinghub.elsevier.com/retrieve/pii/S1350630717300894.
[68] E. Wycisk, A. Solbach, S. Siddique, D. Herzog, F. Walther, C. Emmelmann, Effects of defects in laser additive manufactured ti-6al-4v on fatigue properties, 56 371–378, https://doi.org/10.1016/j.phpro.2014.08.120, https://linkinghub.elsevier.com/retrieve/pii/S187538921400265X.
[69] R. Caivano, A. Tridello, G. Chiandussi, G. Qian, D. Paolino, F. Berto, Very high cycle fatigue (VHCF) response of additively manufactured materials: a review, 44 (11) 2919–2943, https://doi.org/10.1111/ffe.13567, https://onlinelibrary.wiley.com/doi/10.1111/ffe.13567.
[70] A. Tridello, C. Biffi, J. Fiocchi, P. Bassani, G. Chiandussi, M. Rossetto, A. Tuissi, D. Paolino, VHCF response of as-built SLM AlSi10mg specimens with large loaded volume, 41 (9) 1918–1928, https://doi.org/10.1111/ffe.12830, https://onlinelibrary.wiley.com/doi/10.1111/ffe.12830.
[71] Y. Murakami, Effect of hardness HV on fatigue limits of materials containing defects, and fatigue limit prediction equations, in: Metal Fatigue, Elsevier, pp. 57–74, https://doi.org/10.1016/B978-008044064-4/50005-0, https://linkinghub.elsevier.com/retrieve/pii/B9780080440644500050.
[72] Y. Murakami, Material defects as the basis of fatigue design, 41 2–10, https://doi.org/10.1016/j.ijfatigue.2011.12.001, https://linkinghub.elsevier.com/retrieve/pii/S0142112311003161.
[73] M. Cao, Y. Liu, F.P. Dunne, A crystal plasticity approach to understand fatigue response with respect to pores in additive manufactured aluminium alloys, 161 106917, https://doi.org/10.1016/j.ijfatigue.2022.106917, https://linkinghub.elsevier.com/retrieve/pii/S0142112322001864.
[74] F.P.E. Dunne, Fatigue crack nucleation: mechanistic modelling across the length scales, 18 (4) 170–179, https://doi.org/10.1016/j.cossms.2014.02.005, https://www.sciencedirect.com/science/article/pii/S1359028614000151.
[75] Y. Xu, W. Wan, F.P.E. Dunne, Microstructural fracture mechanics: stored energy density at fatigue cracks, 146 104209, https://doi.org/10.1016/j.jmps.2020.104209, https://www.sciencedirect.com/science/article/pii/S0022509620304300.
[76] M. Awd, L. Saeed, F. Walther, Quantum mechanical-based fracture behavior of l-PBF/SLM ti-6al-4v in the very high cycle fatigue regime, 12 (2) 20220085, https://doi.org/10.1520/MPC20220085, http://www.astm.org/doiLink.cgi?MPC20220085.
[77] M. Awd, L. Saeed, F. Walther, A review on the enhancement of failure mechanisms modeling in additively manufactured structures by machine learning 151 107403, 151 107403, https://doi.org/10.1016/j.engfailanal.2023.107403, https://www.sciencedirect.com/science/article/pii/S1350630723003576.
[78] A. Nammalvar Raja Rajan, M. Krochmal, M. Shahmardani, T. Wegener, A. Hartmaier, T. Niendorf, G. Moeini, Micromechanical modeling of the low-cycle fatigue behavior of additively manufactured AlSi10mg, 879 145232, https://

doi.org/10.1016/j.msea.2023.145232, https://www.sciencedirect.com/science/article/pii/S0921509323006561.
[79] D.-F. Li, R.A. Barrett, P.E. O'Donoghue, N.P. O'Dowd, S.B. Leen, A multi-scale crystal plasticity model for cyclic plasticity and low-cycle fatigue in a precipitate-strengthened steel at elevated temperature, 101 44–62, https://doi.org/10.1016/j.jmps.2016.12.010, https://www.sciencedirect.com/science/article/pii/S0022509616302241.
[80] E08 Committee, Test method for measurement of fatigue crack growth rates, https://doi.org/10.1520/E0647-15E01, http://www.astm.org/cgi-bin/resolver.cgi?E647-15E1.
[81] S. Bhattacharya, K. Sharma, Fatigue crack growth simulations of FGM plate under cyclic thermal load by XFEM, 86 727–731, https://doi.org/10.1016/j.proeng.2014.11.091, https://linkinghub.elsevier.com/retrieve/pii/S1877705814020505.
[82] S. Bhattacharya, I.V. Singh, B.K. Mishra, T.Q. Bui, Fatigue crack growth simulations of interfacial cracks in bi-layered FGMs using XFEM, 52 (4) 799–814, https://doi.org/10.1007/s00466-013-0845-8, http://link.springer.com/10.1007/s00466-013-0845-8.
[83] M. Kumar, I. Singh, B. Mishra, Fatigue crack growth simulations of plastically graded materials using XFEM and j-integral decomposition approach, 216 106470, https://doi.org/10.1016/j.engfracmech.2019.05.002, https://linkinghub.elsevier.com/retrieve/pii/S0013794419302723.
[84] H. Dirik, T. Yalçinkaya, Fatigue crack growth under variable amplitude loading through XFEM, 2 3073–3080, https://doi.org/10.1016/j.prostr.2016.06.384, https://linkinghub.elsevier.com/retrieve/pii/S2452321616304024.
[85] J. Mayeur, D. McDowell, A three-dimensional crystal plasticity model for duplex ti–6al–4v, 23 (9) 1457–1485, https://doi.org/10.1016/j.ijplas.2006.11.006, https://linkinghub.elsevier.com/retrieve/pii/S0749641906001574.
[86] D. Zhou, X. Wang, R. Wang, T. Zhang, X. Yang, Y. Jiang, X. Zhang, J. Gong, S. Tu, An extended crystal plasticity model to simulate the deformation behaviors of hybrid stress–strain controlled creep-fatigue interaction loading, 156 106680, https://doi.org/10.1016/j.ijfatigue.2021.106680, https://www.sciencedirect.com/science/article/pii/S0142112321005223.
[87] K. Somlo, K. Poulios, C. Funch, C. Niordson, Anisotropic tensile behaviour of additively manufactured ti-6al-4v simulated with crystal plasticity, 162 104034, https://doi.org/10.1016/j.mechmat.2021.104034, https://linkinghub.elsevier.com/retrieve/pii/S016766362100260X.
[88] K. Somlo, B. Frodal, C. Funch, K. Poulios, G. Winther, O. Hopperstad, T. Børvik, C. Niordson, Anisotropic yield surfaces of additively manufactured metals simulated with crystal plasticity, 94 104506, https://doi.org/10.1016/j.euromechsol.2022.104506, https://linkinghub.elsevier.com/retrieve/pii/S0997753822000031.
[89] R. Bandyopadhyay, S.E. Gustafson, K. Kapoor, D. Naragani, D.C. Pagan, M.D. Sangid, Comparative assessment of backstress models using high-energy X-ray diffraction microscopy experiments and crystal plasticity finite element simulations, 136 102887, https://doi.org/10.1016/j.ijplas.2020.102887, https://www.sciencedirect.com/science/article/pii/S0749641920302370.
[90] T. Hochrainer, S. Sandfeld, M. Zaiser, P. Gumbsch, Continuum dislocation dynamics: towards a physical theory of crystal plasticity, 63 167–178, https://doi.org/10.1016/j.jmps.2013.09.012, https://www.sciencedirect.com/science/article/pii/S0022509613001877.
[91] M. Maltamo, A. Kangas, J. Uuttera, T. Torniainen, J. Saramäki, Comparison of percentile based prediction methods and the Weibull distribution in describing the diameter distribution of heterogeneous Scots pine stands, 133 (3) 263–274, https://doi.org/10.1016/S0378-1127(99)00239-X, https://linkinghub.elsevier.com/retrieve/pii/S037811279900239X.
[92] J. Liu, F. Hua, S. Lang, Y. Ran, R. Zi, Evaluation of fatigue strength on multiaxial notched specimenss considering failure probability, 156 106649, https://doi.org/10.1016/j.ijfatigue.2021.106649, https://linkinghub.elsevier.com/retrieve/pii/S0142112321004928.
[93] S. Glodež, M. Šori, J. Kramberger, Prediction of micro-crack initiation in high strength steels using Weibull distribution, 108 263–274, https://doi.org/10.1016/j.engfracmech.2013.02.015, https://linkinghub.elsevier.com/retrieve/pii/S001379441300057X.
[94] M. Muniz-Calvente, A. Fernández-Canteli, B. Pyttel, E. Castillo, Probabilistic assessment of VHCF data as pertaining to concurrent populations using a Weibull regression model, 40 (11) 1772–1782, https://doi.org/10.1111/ffe.12641, https://onlinelibrary.wiley.com/doi/10.1111/ffe.12641.
[95] H.W. Ahmad, J.H. Hwang, K. Javed, U.M. Chaudry, D.H. Bae, Probabilistic fatigue life prediction of dissimilar material weld using accelerated life method and neural network approach, 7 (1) 10, https://doi.org/10.3390/computation7010010, http://www.mdpi.com/2079-3197/7/1/10.
[96] A. Barto, M. Duff, Monte Carlo matrix inversion and reinforcement learning, in: J. Cowan, G. Tesauro, J. Alspector (Eds.), Advances in Neural Information Processing Systems, vol. 6, Morgan-Kaufmann, https://proceedings.neurips.cc/paper/1993/file/3b3dbaf68507998acd6a5a5254ab2d76-Paper.pdf.
[97] P. Abbeel, A.Y. Ng, Apprenticeship learning via inverse reinforcement learning, in: Twenty-first international conference on Machine learning - ICML '04, ACM Press, p. 1., https://doi.org/10.1145/1015330.1015430, http://portal.acm.org/citation.cfm?doid=1015330.1015430.
[98] J.M. Combes, P. Duclos, R. Seiler, The Born-Oppenheimer approximation, in: G. Velo, A. S. Wightman (Eds.), Rigorous Atomic and Molecular Physics, NATO Advanced Study Institutes Series, Springer US, pp. 185–213, https://doi.org/10.1007/978-1-4613-3350-0_5.
[99] T. Ziegler, A. Rauk, On the calculation of bonding energies by the hartree fock slater method, 46 (1) 1–10, https://doi.org/10.1007/BF00551648.
[100] W. Kohn, L.J. Sham, Self-consistent equations including exchange and correlation effects, 140 (4) A1133–A1138, publisher: American Physical Society, https://doi.org/10.1103/PhysRev.140.A1133, https://link.aps.org/doi/10.1103/PhysRev.140.A1133.
[101] D.S. Sholl, J.A. Steckel, Density functional theory: a practical introduction, Wiley, OCLC, ocn245025462.
[102] W. Eitel, K. Jost, J. Kessler, Polarization of slow electrons by hg and range of applicability of the relativistic hartree potential, 159 (1) 47–49, publisher: American Physical Society, https://doi.org/10.1103/PhysRev.159.47, https://link.aps.org/doi/10.1103/PhysRev.159.47.
[103] M.K. Harbola, V. Sahni, Quantum-mechanical interpretation of the exchange-correlation potential of Kohn-Sham density-functional theory, 62 (5) 489–492, publisher: American Physical Society, https://doi.org/10.1103/PhysRevLett.62.489, https://link.aps.org/doi/10.1103/PhysRevLett.62.489.
[104] G. Kresse, D. Joubert, From ultrasoft pseudopotentials to the projector augmented-wave method, 59 (3) 1758–1775, https://doi.org/10.1103/PhysRevB.59.1758, https://link.aps.org/doi/10.1103/PhysRevB.59.1758.